Bioactive Materials 9 (2022) 491–507

Contents lists available at ScienceDirect

Bioactive Materials

journal homepage: www.sciencedirect.com/journal/bioactive-materials

Fabrication of a bio-instructive scaffold conferred with a favorable microenvironment allowing for superior implant osseointegration and accelerated in situ vascularized bone regeneration via type H vessel formation

Yijun He [a,1], Wenhao Wang [a,1], Shaozhang Lin [a,1], Yixi Yang [a], Lizhi Song [a], Yihan Jing [a], Lihao Chen [a], Zaopeng He [b], Wei Li [b], Ao Xiong [c,d], Kelvin W.K. Yeung [e,f], Qi Zhao [a], Yuan Jiang [a], Zijie Li [a], Guoxian Pei [g,**], Zhi-Yong Zhang [a,h,i,*]

[a] Translational Research Centre of Regenerative Medicine and 3D Printing of Guangzhou Medical University, Guangdong Province Engineering Research Center for Biomedical Engineering, State Key Laboratory of Respiratory Disease, The Third Affiliated Hospital of Guangzhou Medical University, Guangzhou, 510150, PR China
[b] Hand and Foot Surgery & Plastic Surgery, Affiliated Shunde Hospital of Guangzhou Medical University, Foshan, 528315, PR China
[c] Department of Bone & Joint Surgery, Peking University Shenzhen Hospital, Shenzhen, 518036, PR China
[d] National & Local Joint Engineering Research Center of Orthopaedic Biomaterials, Peking University Shenzhen Hospital, Shenzhen, 518036, PR China
[e] Department of Orthopaedics and Traumatology, The University of Hong Kong, Pokfulam, Hong Kong, 999077, PR China
[f] Shenzhen Key Laboratory for Innovative Technology in Orthopaedic Trauma, The University of Hong Kong Shenzhen Hospital, Shenzhen, 518053, PR China
[g] The Third Affiliated Hospital of Southern University of Science and Technology, Southern University of Science and Technology, Shenzhen, 518055, PR China
[h] Department of Orthopaedic Surgery, The Third Affiliated Hospital of Guangzhou Medical University, Guangzhou, 510150, PR China
[i] Medical Technology and Related Equipment Research for Spinal Injury Treatment, City Key Laboratory, The Third Affiliated Hospital of Guangzhou Medical University, Guangzhou, 510150, PR China

ARTICLE INFO

Keywords:
Cell-derived decellularized extracellular matrix
Microenvironment
Vascularized bone regeneration
Type H vessels
Osseointegration

ABSTRACT

The potential translation of bio-inert polymer scaffolds as bone substitutes is limited by the lack of neovascularization upon implantation and subsequently diminished ingrowth of host bone, most likely resulted from the inability to replicate appropriate endogenous crosstalk between cells. Human umbilical vein endothelial cell-derived decellularized extracellular matrix (HdECM), which contains a collection of angiocrine biomolecules, has recently been demonstrated to mediate endothelial cells(ECs) – osteoprogenitors(OPs) crosstalk. We employed the HdECM to create a PCL (polycaprolactone)/fibrin/HdECM (PFE) hybrid scaffold. We hypothesized PFE scaffold could reconstitute a bio-instructive microenvironment that reintroduces the crosstalk, resulting in vascularized bone regeneration. Following implantation in a rat femoral bone defect, the PFE scaffold demonstrated early vascular infiltration and enhanced bone regeneration by microangiography (μ-AG) and micro-computational tomography (μ-CT). Based on the immunofluorescence studies, PFE mediated the endogenous angiogenesis and osteogenesis with a substantial number of type H vessels and osteoprogenitors. In addition, superior osseointegration was observed by a direct host bone-PCL interface, which was likely attributed to the formation of type H vessels. The bio-instructive microenvironment created by our innovative PFE scaffold made possible superior osseointegration and type H vessel-related bone regeneration. It could become an alternative solution of improving the osseointegration of bone substitutes with the help of induced type H vessels, which could compensate for the inherent biological inertness of synthetic polymers.

Peer review under responsibility of KeAi Communications Co., Ltd.

* Corresponding author. Translational Research Centre of Regenerative Medicine and 3D Printing, Guangzhou Medical University, Guangdong Province Engineering Research Center for Biomedical Engineering The South China Branch of National Tissue Engineering Center of China, The State Key Laboratory of Respiratory Disease, The Third Affiliated Hospital of Guangzhou Medical University.

** corresponding author. The Third Affiliated Hospital of Southern University of Science and Technology.

E-mail addresses: nfperry@163.com (G. Pei), mr.zhiyong@gmail.com (Z.-Y. Zhang).

[1] these authors contributed equally to this work.

https://doi.org/10.1016/j.bioactmat.2021.07.030
Received 29 March 2021; Received in revised form 2 July 2021; Accepted 26 July 2021
Available online 12 August 2021

1. Introduction

Besides autologous and allogenic bone grafting, which carries significant comorbidities such as disease transmission and adverse immune reaction risks, tissue engineering (TE) using polymeric bone substitute has emerged as an appealing alternative in treating bone defects from various etiologies [1,2]. However, classic cell-based TE, which relies on the seeding of autologous or allogenous cells onto biodegradable scaffolds followed by a period of in vitro cultivation before surgical implantation, has several limitations, including a time-consuming cell expansion process, low cell survival upon implantation, and the possible short- and long-term immune-rejection [3]. To circumvent these shortcomings, acellular bioactive bone scaffolds were studied as an alternative. The cell-free scaffolds, made of synthetic biodegradable polymers, can be available off the shelf without a lengthy process of cell handling and storage, aiming to regenerate the bone by creating healing microenvironments and control host cell behavior [4]. However, given the attributes of biological inertness they all have in common, polymer scaffolds still face challenges with inadequate neovascularization and insufficient host osseointegration before a successful clinical translation [2,5,6].

In general, bone regeneration relies highly on adequate vasculature that transfers oxygen and nutrients and removes metabolites [7]. Early scaffold neovascularization facilitates cell proliferation, tissue ingrowth followed by subsequent bone mineralization and regeneration, while scarce vascular infiltration and hypoxia lead to central necrosis or failed osseointegration manifesting as fibrous encapsulation [8,9]. Various fabrication methods have been attempted to improve the scaffolds' bio-activeness to counteract the nature of inertness possessed by synthetic polymers [10–14]. Scaffolds, either physio-chemically modified, blended with organic or inorganic compounds, or loaded with bioactive ingredients, were used to create a microenvironment attempting to recruit, regulate local stem cells to achieve in situ vascularized bone regeneration and better implant osseointegration [6,15,16]. For instance, local coupled angiogenesis and osteogenesis of scaffold implant was achieved by the addition of recombinant vascular endothelial growth factor (VEGF) and bone morphogenetic protein (BMP) [8,17–19] However, growth factors (GFs) failed to recapitulate the intricacy of the local regenerative microenvironment, leading to osteal and vascular malformation [20].

It is crucial to reintroduce a microenvironment that can recapitulate successful endothelial cell-osteoblast (EC-OP) crosstalk in the process of vascularized bone regeneration [21–23]. Recent investigations have suggested the role of vascular endothelial extracellular matrix (ECM), with a majority from human umbilical vein endothelial cell (HUVEC), as a substrate in mediating the crosstalk between ECs and OPs, which couples angiogenesis and osteogenesis [23–26]. Human mesenchymal stem cells (hMSCs) or osteoblasts exhibited favorable osteogenesis and increased metabolic activity when cultured on HUVEC-derived decellularized ECM (HdECM) [24,25]. Though the underlying mechanism has yet to be clarified, some evidence might explain by revealing that HdECM was determinant of MSC's fate, that cells from exfoliated deciduous teeth (SHED) were induced into endothelial lineage when being cultured on HdECM [26]. In vitro, HdECM treated-MSCs also promoted angiogenesis by an enhanced formation of branching networks [25]. Through mechanisms of cell-matrix interactions, HdECM orchestrates the mechanical, growth factor, and angiocrine signals necessary for cell proliferation and differentiation, suggesting its potential to be a tissue-specific niche useful for regenerative medicine [23,27–29]. In vitro studies hint at the possibility that HdECM, which possesses a complete collection of angiocrine biomolecules for guiding both angiogenesis and osteogenesis, could be a potent substrate to engineer a bio-instructive microenvironment for promoting in situ vascularized bone regeneration and thereby enhancing implant osseointegration, which has yet to be studied in vivo.

Researchers have explored 3D-printing technology for decades in order to produce biodegradable polymer bone implants with optimum mechanical strength, tunable porosity, and certain levels of bioactivity [14]. Here, we present a 3D-printed polycaprolactone (PCL) scaffold spatiotemporally incorporated with HdECM/fibrin hybrid gel to engineer a bio-instructive microenvironment for accelerated in situ vascularized bone regeneration. Initially, we proved the hypothesis that HdECM, as a substrate, could enhance angiogenesis and osteogenesis in vitro. By incorporating HdECM/fibrin gel into the biodegradable PCL scaffold's pores, we showed that the hybrid scaffold achieved rapid vascular infiltration in a subcutaneous implantation model and enhanced bone regeneration in a rat femoral defect site, particularly within the central region. Immunofluorescence histology showed that the scaffold's microenvironment mediated the formation of type H vessels, a subtype of capillary coupled with osterix-positive osteoprogenitor cells [30–32]. Besides, HIF-1A was upregulated in the scaffold-mediated microenvironment. The functionalization of PCL scaffold with HdECM/fibrin gel had achieved vascularized bone regeneration and subsequently enhanced PCL's osseointegration, as demonstrated by a scarce formation of peri-implant fibrous encapsulation. The present work demonstrated a novel strategy that rapid type H vessel angiogenesis and osteogenesis mediated by the microenvironment might be favorable for enhanced osseointegration of polymer implants.

2. Method

1. Isolation of HUVECs and generation of HUVEC-derived decellularized ECM

Primary HUVECs were obtained from umbilical cords taken after delivery of healthy term newborns with approval from the Ethics Committee of The Third Affiliated Hospital of Guangzhou Medical University. Isolation and characterization of primary HUVECs were performed as described with mild modifications [33,34]. Briefly, after the umbilical vein was bluntly dissected from the cord, the lumen was flushed with phosphate buffer solution (PBS) to remove residual blood followed by an infusion of 0.2% collagenase solution and a subsequent incubation for 10 min at 37 °C. Cells were centrifuged at 250g for 5 min before seeding. HUVECs were isolated and cultured at 37 °C, 5% CO_2 in Endothelial Cell Medium (Sciencell, US) containing 5% fetal bovine serum, 100U/ml penicillin, 100 μg/ml streptomycin, and 1% Endothelial Cell Growth (Sciencell, US). The medium was changed every 3 days. HUVECs between passage 5 to 6 were used for the generation of dECM as previously described [26]. Cells were cultured for an additional five days after confluence was reached. Later on, cells were treated with a mixture solution of 0.5% Triton X-100 and 20 mM NH_4OH for 5 min as previously denoted, followed by the treatment of Dnase I (100U/ml) for 45 min. The HUVEC-derived CD-dECM (HdECM) was washed with deionized water five times and lyophilized before subsequent use. As a control, HUVEC-derived ECM without decellularization (HECM) was collected by scaping the cell-sheet off the culture surface.

2. Characterization of HUVEC-derived dECM

To characterize the extracellular matrix's major components, both HdECM and HECM were fixed in 4% paraformaldehyde for 30 min, embedded in paraffin, and sectioned. Slides were stained with HE, Masson, Safranin O, and Picrosirius Red. Immunofluorescence staining was also performed. Sections were incubated with primary antibodies against collagen I (ab6308, 1:200, Abcam, UK), laminin (ab268079, 1:100, Abcam), and fibronectin (F7387, 1:200, Sigma) at 4 °C overnight followed by incubation with secondary antibodies for 1 h and with DAPI for 5 min. Images were taken using fluorescence microscopy (Olympus Imaging Systems, Japan). To characterize the protein within HdECM, 10 μg protein extract mixed with 4 × loading buffer was loaded into a 1.5 mm 4%–12% gradient SDS-PAGE gel. SDS-PAGE was performed at 120 V for at least 100 min. The gel was stained with Coomassie Blue

overnight and destained in deionized H2O containing 10% acetic acid and 40% ethanol for 2 h. Visualization of the bands was carried out on a GE Image Scanner III densitometer, and the image was taken using ImageQuant TL software (GE Healthcare). LC/MS was performed to identify peptide sequences of the HdECM (n = 3). The samples were homogenized in a 4% SDS and 100 mM dithiothreitol (DTT) and lysed by a filter-aided sample preparation protocol. Proteins were classified by Gene Ontology (GO) annotation based on the categories of "biological processes," "cellular components," and "molecular functions." To quantify the removal of nucleic content, DNA was extracted with a Genomic DNA Kit (Solabio, China), and the concentration was measured from the absorbance at 260 nm by a Nanodrop device (Thermofisher, US).

3. Preparation of Soluble HdECM

HdECM was solubilized by pepsinization as previously described [35,36]. Briefly, HdECM was digested with 0.1% pepsin (w/v) in 0.01 N HCl in a 37 °C water bath for 48 h till a clear solution was obtained. The final solution was neutralized using 0.5 M NaOH to reach a pH of 7.4, followed by osmolarity adjustment using 10X PBS solution to obtain a concentration at 10 mg/ml. The soluble HdECM was kept at −20 °C until further use. The soluble HdECM was used for all subsequent experiments.

4. Cell Culture

HUVECs were obtained and cultured as aforementioned. For cytological analyses, HUVECs were cultured in Endothelial Cell Medium (Sciencell, US) containing 5% fetal bovine serum, 100U/ml penicillin, 100 μg/ml streptomycin, and without the addition of ECGS. Human bone mesenchymal stem cells (hBMSCs) were purchased from Cyangen (China) and cultured at 37 °C and 5% CO_2 in DMEM/F12 supplemented with 10% FBS, 1% Glutamax®(Gibco, US) and 1% 100X penicillin/streptomycin (Thermofisher, US). All cells at passage 6 were used for cytological analyses.

5. Angiogenesis and Osteogenesis of HdECM

A Cell Counting Kit-8 Assay (CCK-8; Dojindo Laboratories, Japan) of hBMSCs and HUVECs was performed to determine the optimal concentration of HdECM. hBMSCs and HUVECs were seeded at a density of 1×10^3 per well on a 96-well-plate, HdECM was supplemented to the culture medium with a final solution of 5 μg/ml, 10 μg/ml, 50 μg/ml, and 100 μg/ml. Cells with incubated with CCK-8 for 3hrs at 37 °C and detected the absorbance at 450 nm. HdECM was supplemented at a concentration of 100 μg/ml in the culture medium for the subsequent assays, while the medium without HdECM served as the control. A wound-healing assay of HUVEC was performed using a Culture-Insert (iBidi, Germany) with an original scratch width of 500 μm according to the manufacturer's protocol. Cell migration was denoted by the healing percentage: (500 μm – new width of scratch)/500 μm × 100%. Tube formation was assessed by culturing HUVEC on Matrigel (Corning, US). Cells were seeded on a Matrigel layer at a density of 5×10^4 per well within 48-well-plates. Tube formation at 6 and 12 h was analyzed by quantifying the number of nodes, number of junctions, and total tube length per high-powered field. hBMSCs were at 80% confluence were changed with osteoinductive media (OM, DEME low glucose with 10% FBS, 50 mg/L ascorbic acid, 10 mmol/l sodium β-glycerophosphate, 1×10^{-7} mol/l dexamethasone) with and without the supplementation of HdECM. At different time points (3, 7, and 14 days), cells at day 3 and 7 were stained with an ALP staining kit (Solarbio, China), while cells at day 14 were stained with 1% (wt/v) Alizarin Red S (ARS, Solarbio, China) at pH 4.2. On day 7, cells were lysed using 100 μl RIPA lysis buffer. The alkaline phosphatase (ALP) activity of the cell lysate was evaluated with the ALP kit (Beyotime, China) per the manufacturer's instruction. After the incubation with p-nitrophenol for 5 min, the absorbance was measured at 405 nm. ALP levels were determined by the absorbance normalized to total protein content determined by the bicinchoninic acid (BCA) Protein Assay Kit (Solarbio, China). To quantify ARS as previously described [13], air-dried ARS-stained cell samples were incubated with 10% acetic acid overnight and centrifuged for 15 min at 20,000g. The supernatant was neutralized with 10% ammonium hydroxide. A 100 μl of each sample was added to 96-well-plates and measured at a wavelength of 405 nm with a microplate reader. All studies were performed in triplicate. Student t-test was used to determine the statistical significance (P-value) of the obtained data.

6. RNA Isolation and Quantitative Real-Time Polymerase Chain Reaction (qPCR)

According to the manufacturer's instructions, total RNA from all in vitro experiments was extracted using the Trizol reagent (Invitrogen, US). Complementary DNA was synthesized from 1 μg total RNA using Revertaid reverse transcriptase (Thermofisher, US) following the manufacture's protocol. After reverse transcription reaction, rt-PCR was performed using AceQ Universal SYBR qPCR Master Mix (Vazyme, China) and an ABI Step One Plus Real-Time PCR System (Applied Biosystem, US). Each sampled was performed in triplicate and GAPDH, and β-actin was used as reference. Student t-test was used to determine the statistical significance (P-value) of the obtained data. The primer sequences used were described in Supplementary Table 1.

7. Ex Vivo Angiogenesis Assay of Fibrin Gel and Fibrin/HdECM Gel

Rat aortic assay was performed as described [37]. Briefly, the descending aortae were dissected from Sprague-Dawley (SD) rats weighing 75–80 g. The vessel was cut into 1 mm long rings with the fibro-adipose tissue and collateral vessels removed. At 4 °C, 300 μL of ungelled fibrin or fibrin/HdECM solution was added onto each well of 24-well-plates. The aortic rings were submerged within the ungelled solution. Subsequently, the plate was incubated at 37 °C for 30 min for gelation. 1 ml of Endothelial Cell Medium supplemented with 5% FBS, 100U/ml penicillin, 100 μg/ml streptomycin was added to each well. All samples were cultured at 37 °C and 5% CO_2. On day 3, 5, 7, the median length of microvessel sprouting was measured. Then, samples were fixed with 4% PFA, penetrated with 0.25% Triton-X100 in PBS for 20 min before the staining using Actin-Tracker (Beyotime, China) and DAPI (Beyotime). A laser scanning confocal microscope (LSCM, Nikon) was used for photography. The experiment was performed in triplicate. Student t-test was used to determine the statistical significance (P-value) of the obtained data.

8. Fabrication of PCL/Fibrin/HdECM Hybrid Scaffold

The 3D-printed scaffold was fabricated using a 3D-bioplotter (EnvisionTEC, Germany). In the high-temperature module, PCL pellets (Mw 80,000, Sigma-Aldrich) were air-dried at 37 °C overnight, loaded into a stainless steel cartridge connecting with a metal tip in 300 μm diameter, and heated to 140 °C for 6 h. The pneumatic pressure was set at 3.5 ± 0.5 bar, and the deposition speed of 0.2 ± 0.1 mm/s was set. The platform temperature was set at 20 °C. PCL strands were deposited with a 0-60-120° in successive layer patterns as previously described [38]. PCL cylindrical scaffolds (14 mm in diameter, 1.2 mm in thickness for in vitro analyses, 14 mm in diameter and 5 mm in thickness for in vivo bone defect, respectively) were generated using Bioplotter RP and VisualMachines software (EnvisionTEC) [39,40]. All For sterilization, PCL scaffolds were immersed within isopropanol for 30 min twice and underwent UV radiation for 30 min. The preparation of fibrin/HdECM gel was achieved by mixing fibrinogen solution (10 mg/ml, Sigma), HdECM (10 mg/ml) and thrombin solution (100 U/ml) in 10:10:1 proportion. As a control, fibrin gel was produced by mixing fibrinogen solution (10

mg/ml, Sigma), PBS and thrombin solution (100 U/ml) in 10:10:1 proportion. Hybrid scaffolds were made by quickly filling the mixed solution into the pores of PCL scaffolds using a custom-made device before being transferred to 37°Cfor 30 min until polymerization was termed. Scaffold with pure PCL, PCL/Fibrin, and PCL/Fibrin/HdECM scaffold were termed PP, PF, and PFE, respectively, in the subsequent tests.

9. Morphological Characterization of Hybrid Scaffolds

The gross view of the hybrid scaffold was obtained by a dissecting microscope (Zeiss). The hybrid scaffolds were lyophilized and bisected with a surgical blade to reveal the cross-sectional area before the scanning electron microscope (SEM, Zeiss Merlin) morphological assessment. Before obtaining the SEM images, the scaffolds were sputtered-coated with a thin layer of gold. The operating voltage was set at 5 kV.

10. Cell Viability, Proliferation, Chemotaxis, and Osteogenesis of Hybrid Scaffolds

As aforementioned, scaffolds (ϕ14mm, 1.2 mm in thickness) were used for in vitro studies. PP, PF, and PFE scaffolds were placed into wells in ultra-low attachment surface 24-well-plates (Corning). 2×10^5 hBMSCs resuspended in 150 μl were seeded onto each scaffold and incubated for 3 h. Then, wells were added up with a complete culture medium to 1 ml and cultured at 37 °C and 5% CO_2. At 72 h, cell viability assay was performed using a Live/Dead Staining Kit (Beyotime, China) per instruction. Samples were incubated with the Calcein AM/PI solution at room temperature for 30 min before being photographed with an inverted fluorescence microscope (Olympus, Japan) at an absorbance of 494 nm for live cells, 528 nm for dead cells. The proliferation of hBMSCs cultured on the hybrid scaffold was assessed by a CCK-8 kit (Beyotime). At different time points (day1–5), scaffolds were rinsed with PBS and incubated with the 10% CCK-8 solution in DMEM/F12 at 37 °C for 90 min. The supernatant was measured at an absorbance of 450 nm with a microplate reader. For the chemotactic assay, 2.5×10^4 hBMSCs were seeded in upper chambers in a transwell insert system with a pore size of 8 μm while scaffolds were placed in the lower chamber. Supplement- and serum-free DMEM/F12 were used as the culture medium. At 24 h, cells on the reverse side of the insert were stained with 1.0% (w/v) crystal violet (Solarbio, China) and photographed with an inverted microscope (Nikon, Japan) and a dissecting microscope (Zeiss). On day 4, the medium was replaced by OM, and the scaffolds were cultured with hBMSCs for an additional 14 days. ARS staining was performed to evaluate the osteogenesis of hBMSCs cultured on hybrid scaffolds. Briefly, fixed scaffolds were stained with 1% ARS solution for 30 min. ARS quantification was performed as aforementioned. All studies were performed in triplicate.

11. Angiogenesis of Hybrid Scaffolds in Rat Subcutaneous Implantation Model

All animal experiments were approved by the Animal Ethics Committee of Guangdong Zhongke EnHealth Science and Technology Co., Ltd. Male SD rats (Zhejiang Vital River Laboratory Animal Technology, China) weighing around 200g were anesthetized with an intraperitoneal injection of 4% pentobarbital sodium (40 mg/kg body weight). Each rat received three randomized subcutaneous implants: PP, PF, and PFE. Animals were euthanized on day 7 and 31 post-implantation. Retrieved implants were fixed in 10% neutral formalin for 1 day at 4 °C followed by paraffin embedding. 5 μm thick sectioned for stained for hematoxylin and eosin (HE) and CD31 immunohistochemical analysis. For immunostaining, sections were dewaxed, antigen retrieved, and blocked with 10% goat serum before incubation with primary antibody against CD31 (1:2000, ab182981, Abcam, UK) at 4 °C overnight. The secondary antibody was staining using goat anti-rabbit IgG-HRP (1:2000, ab205718, Abcam). Stains were visualized with DAB (DAB-4033, MXB Biotechnologies, China). Positive CD31 staining was quantified as the total number of vessels per tissue area.

12. Weight-bearing Femur Bone Epicondylar Defect Model and Hybrid Scaffold Implantation

The rat femoral epicondylar defect was used for investigation as previously described [13]. Briefly, 300–350 g SD rats achieved general anesthesia with an intraperitoneal injection of 4% pentobarbital sodium (40 mg/kg body weight). A sterile field was created before local administration of 1% lidocaine. Following the skin incision, the lateral femoral epicondyle was exposed through the intermuscular plane between vastus lateralis and hamstrings. A bicortical tunnel was established with an electric drill mounted with a ϕ3.0 mm drill bit. Thermal necrosis was avoided, and residual bone debris was removed by cold saline irrigation and suctioning during the procedure. The periosteum covering the tunnel was removed before the implantation of scaffolds. Animals were randomly divided into four groups as follows: sham, PP, PF, PFE. Postoperative analgesics (meloxicam) were administered intramuscularly for consecutive 3 days.

13. Radiographic Evaluation

At 0, 2, and 4 weeks, rats were euthanized with CO_2, and femurs were harvested and scanned with a high-resolution micro-CT (SkyScan 1276, Brucker) at an isometric solution 15 μm (85 kV and 200 μA) to evaluate the in vivo osteointegration of the hybrid scaffolds. The region of interest (ROIs) was determined by the size matching with the scaffolds (D:3.0 mm, H:5 mm) and their cylindrical internal region (D:1.5 mm, H:2.5 mm). The bone tissue volume/total tissue volume (BV/TV) was calculated. All tests were repeated with four specimens.

14. Micro-angiography (μ-AG) of Implanted Scaffolds

At 2 weeks, rats (n = 3) from each group were used for micro-angiographic evaluation. After CO_2 euthanization, the rats' abdominal cavity was opened in a quick manner, and the inferior vena cava was severed. Through the cannulation of the descending aorta, the vasculature was flushed with 0.9% cold normal saline containing heparin sodium (100 U/ml), followed by another flush of 10% neutral formalin solution. Then 10 mL of silicone rubber compound (Microfil MV-122; Carver, MA) was injected. Successful perfusion could be defined as the presence of yellow color in both intestinal mucosa and distal limbs. All specimens were stored at 4 °C overnight for optimal silicone rubber polymerization per the manufacturer's instructions. Then, the dissected femurs were again fixed in 10% neutral formalin solution for 48 h followed by decalcification treatment using 10% ethylenediaminetetraacetic acid (EDTA; Sigma, US) solution for 4 weeks. Images were acquired with a high-resolution μ-CT imaging system. The vessel volume within a 3-mm-diameter region surrounding the scaffold region was evaluated.

15. Histological and Immunohistochemical Analysis

Harvested femurs were fixed in 4% paraformaldehyde at 4 °C for 48 h and decalcified in 10% EDTA for four weeks before paraffin embedding. Sections in 5 μm thickness were used for HE and Masson staining. For immunostaining, sections were permeabilized with 0.3% Triton X-100 for 10 min, blocked in 10% goat serum at room temperature for 30 min, and incubated with primary antibodies diluted in 10% goat serum with PBS overnight at 4 °C. The following primary antibodies were used: anti-CD31(ab182981, 1:1000, Abcam), anti-Osterix (ab209484, 1:200, Abcam), anti-Endomucin (sc-65495, 1:100, Santa Cruz), anti-HIF1-α (20960-1-AP, 1:100, Proteintech). After the primary incubation, sections were incubated with appropriate Alexa Fluor-conjugated

secondary antibodies (1:400, Molecular Probes, Life Tech, US) for 1 h at room temperature. Then, coverslips were sealed with DAPI mounting agent and analyzed under an inverted microscope. Mean fluorescent densities were quantified using Image-J software. All tests were repeated with four specimens.

16. Statistical Analysis

All data were demonstrated as mean ± SD. One-way ANOVA with a Turkey post-hos was used for statistical analysis between groups unless indicated otherwise. $P < 0.05$ was considered significant. All quantifications were performed with ImageJ software. Statistical analysis was conducted with GraphPad Prism Software Version 7.0 (GraphPad Software Inc.).

3. Results

1. Characterization of HUVEC-derived decellularized extracellular matrix (HdECM)

Primary HUVECs at passage 5 that cultured for an additional 5 days after confluence presented a typical cobblestone appearance with large dark nuclei (see Fig. 1). After decellularization using 0.5% Triton X-100 and 20 mM NH_4OH and Dnase I, the HdECM showed a fibrillar structure under light microscopy (Fig. 2 (A)). H&E, picrosirius red, and safranin O staining showed an absence of cell nuclei after decellularization, and the fibrillar ECM and its components, including collagens, glycosaminoglycans were preserved (Fig. 2 (B)). To examine the common proteins in ECM, immunofluorescent staining showed that laminin, fibronectin and collagen were partially retained after decellularization. Also, DAPI staining (Fig. 2 (B)) and DNA content quantification (Fig. 2 (E)) revealed that the residual amount of cell nuclei was scarce and lower than 50 ng/mg, indicating the nucleic acid, which has been of consensus to cause immune rejection in vivo [41], was disrupted and removed. The compositions of HdECM were furthered investigated by SDS-PAGE electrophoresis (Fig. 2 (D)). Protein bands over a wide range of molecular weights of the HdECM were exhibited, illustrating that the compositional and biological complexity of the substrates. The combination of Triton X-100, ammonia hydroxide, and Dnase I effectively decellularized the ECM without causing drastic structural and compositional alterations. Proteomic analysis of the HdECM revealed it contained more than 1000 proteins. Bioinformatic analysis of functional enrichment of cellular component showed that HdECM were positively correlated with "extracellular region" and "extracellular space" (Fig. 3 (B)). Molecular function analysis demonstrated that these components took part in the protein binding, including lamin, cadherin, growth factors and extracellular matrix, indicating the potential role in cell migration, cell-matrix adhesion and growth-factor mediated activities (Fig. 3 (C)). Further analysis of biological processes revealed that the components of HdECM significantly correlated with endothelial cell development and differentiation, osteoblast differentiation, cell migration, and metabolic process. Therefore, the HdECM is likely to direct cell fate and eventually contribute to vascularized bone regeneration.

2. Biocompatibility of HdECM as a supplemental substrate

With reference to the previous studies to acquire a soluble or transferrable ECM [35,36], the HdECM underwent a series of treatments until a clear liquid at a 10 mg/ml concentration was obtained. To investigate the effect of HdECM on hBMSCs and HUVECs, HdECM was supplemented in the culture medium at different concentrations. The CCK-8 assay showed that HdECM induced hBMSCs proliferation increased in a dose-dependent manner up to 100 μg/ml from day 2–3 (Fig. 4 (A)). However, HUVECs exhibited a non-significant change in proliferation in response to the supplementation of HdECM, with only an increase of proliferation ($P < 0.05$) at 100 μg/ml at day 3 (Fig. 4 (B)). These

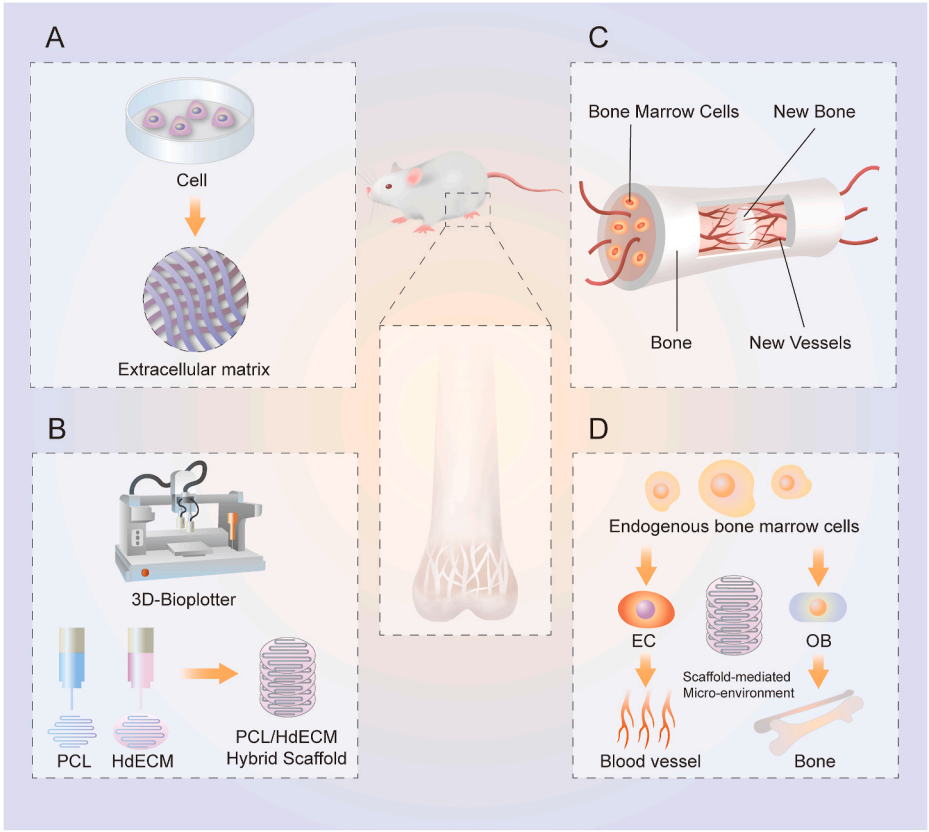

Fig. 1. Schematic demonstration of the fabrication of a 3D-printed hybrid scaffold as an instructive microenvironment for vascularized bone regeneration. A, Diagram showing HUVEC-derived decellularized extracellular matrix (HdECM) was acquired by decellularization of HUVEC monolayer culture. **B,** PCL filament was printed as the framework while fibrin gel or solubilized HdECM/fibrin gel was filled in the space between PCL filaments to fabricate the hybrid scaffolds. **C,** Schematic demonstration showing PCL/fibrin/HdECM scaffold as a bioinstructive microenvironment recruiting endogenous stem cells to achieve angiogenesis and osteogenesis at the site of bone defect. **D,** The cellular mechanism of the hybrid scaffold for vascularized bone regeneration.

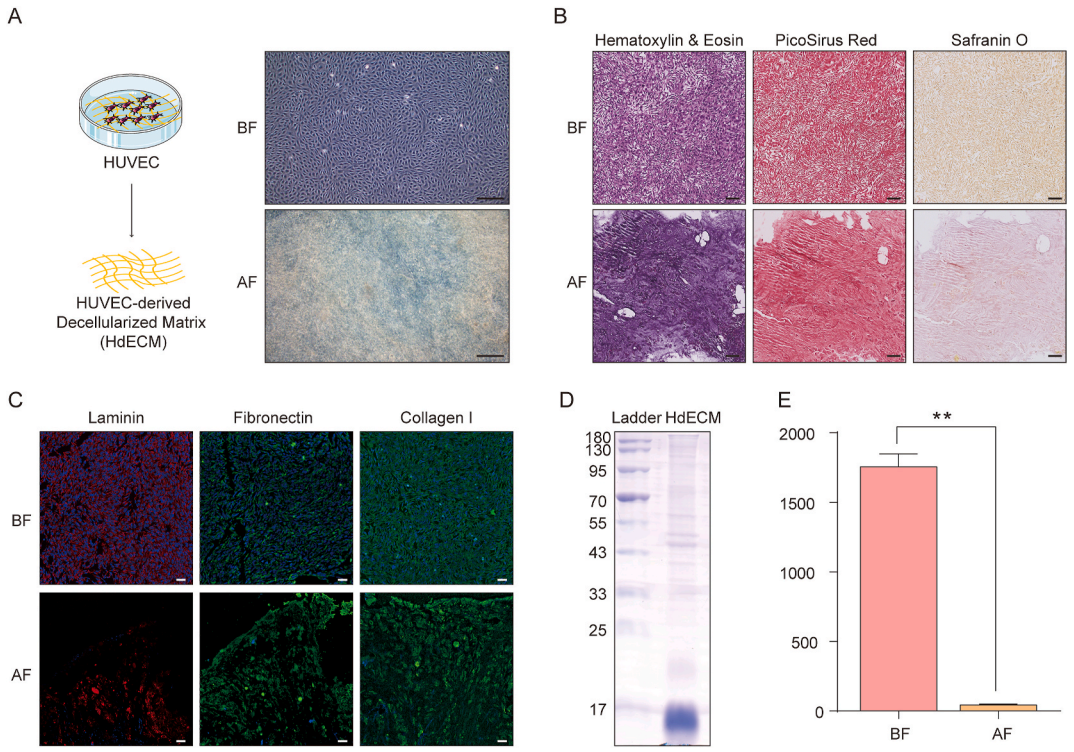

Fig. 2. Characterization of HUVEC-derived decellularized extracellular matrix (HdECM). **A,** Schematic demonstration and morphology of primary HUVEC at passage 5 cultured on TCP before and after decellularization. Scale bars = 200 μm. **B,** Hematoxylin & Eosin, Picosirus Red and Safranin O staining of HUVEC-ECM before and after decellularization. Scale bars = 200 μm. **C,** Immunofluorescent staining images of laminin, fibronectin and collagen I before and after decellularization. Laminin (red), Fibronectin (green), Collagen I (green), DAPI (blue). Scale bars = 200 μm. **D,** SDS-PAGE of protein extracted of HdECM. E, Quantification of DNA content before and after decellularization. * Significant difference, $P < 0.05$; ** Very significant difference, $P < 0.01$; *** Highly significant difference, $P < 0.001$. (For interpretation of the references to color in this figure legend, the reader is referred to the Web version of this article.)

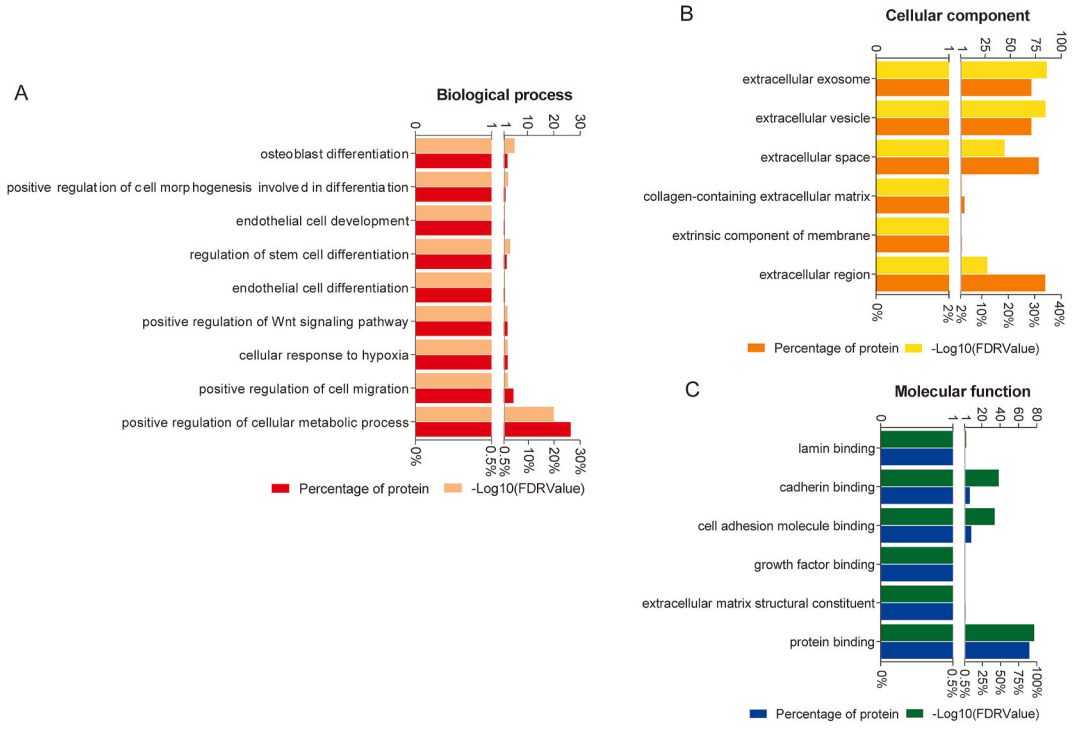

Fig. 3. Proteomic analysis of HdECM (n = 3). **A,** GO analysis of the HdECM proteins involved in various biological processes. **B,** GO analysis of the protein composition. **C,** GO analysis of the molecular functions of HdECM. Pathways were selected based on *P* and expressed as -log (*P*). The threshold marked represents $P = 0.05$.

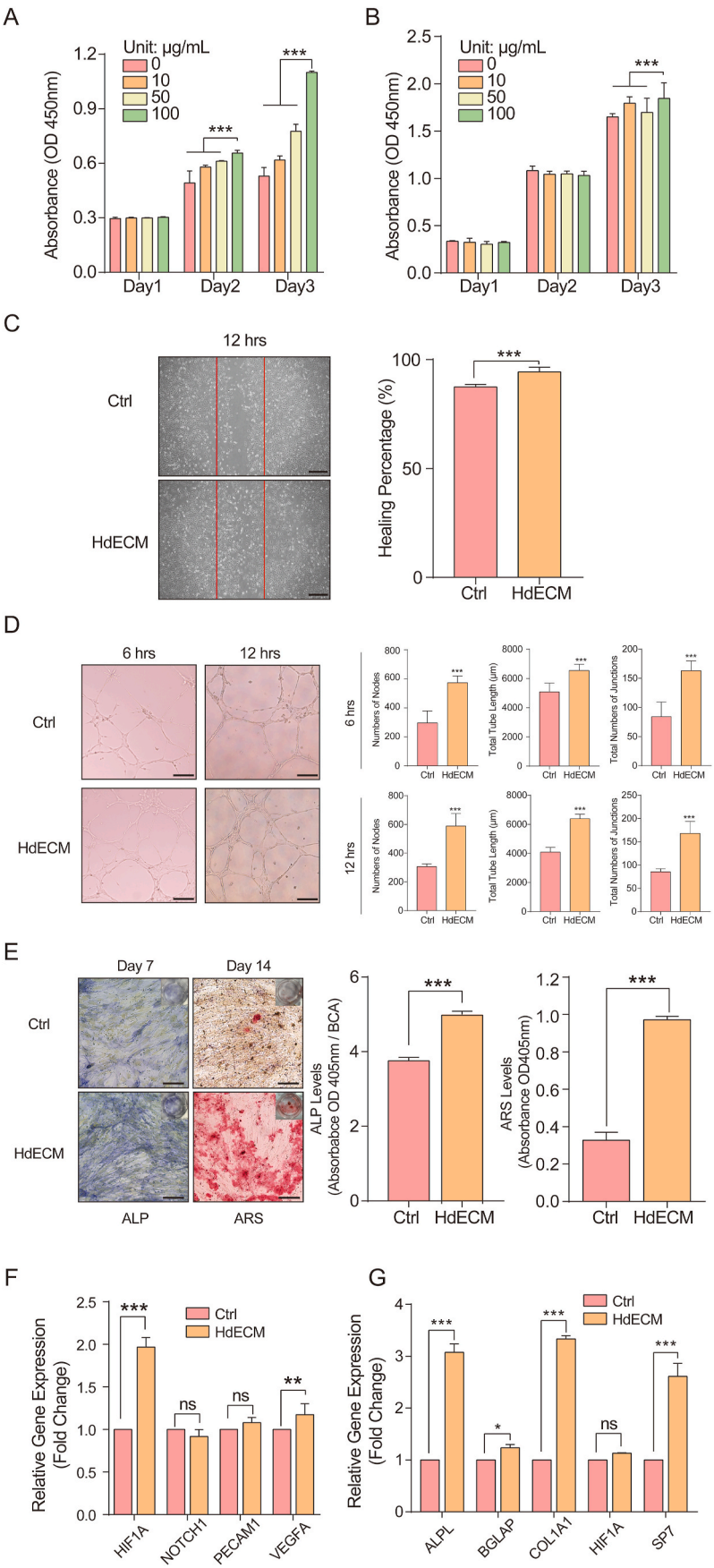

Fig. 4. Assessment of solubilized HdECM's ability to promote angiogenesis and osteogenesis in vitro. **A,** Evaluation of solubilized HdECM on the proliferation of hBMSCs by a CCK-8 assay. **B,** Evaluation of solubilized HdECM on the proliferation of HUVECs by a CCK-8 assay. **C,** Assessment of solubilized HdECM on endothelial cell migration (12 h) assessed by an iBidi cell migration system. Scale bar = 200 μm. **D,** HUVEC tube formation assay (6 and 12 h) and quantification (total numbers of nodes, junctions and the total length of tubes). Scale bar = 200 μm. **E,** Effects of HdECM on the gene expression involving angiogenesis was analyzed by qPCR. **F,** Representative digital images showing the effect of HdECM on the osteogenesis of hBMSCs cultured in osteoinductive medium (OM) by alkaline phosphatase (ALP) and alizarin red S (ARS) staining at different time points, and the quantification of ALP and ARS levels. Scale bars = 200 μm. **G,** Effects of HdECM on osteogenic gene expression of hBMSCs cultured in osteoinductive medium. Scale bars = 200 μm * Significant difference, $P < 0.05$; ** Very significant difference, $P < 0.01$; *** Highly significant difference, $P < 0.001$. (For interpretation of the references to color in this figure legend, the reader is referred to the Web version of this article.)

demonstrated the absence of negative effects on cell proliferation. However, the HdECM might play a different role in mesenchymal stem cells and endothelial cells.

3. In vitro angiogenesis of HdECM

To investigate whether HdECM affects other cytological phenotypes, a HUVEC wound healing assay using iBidi inserts (500 μm interval) was performed. HUVECs demonstrated an increase in migration with HdECM than the control (Fig. 4 (C)). Tube formation assays were performed to investigate the morphogenic effect of HdECM on HUVECs. With the addition of HdECM, HUVECs exhibited a denser vascular network compared to the control at 6 and 12 h. Quantitative analysis including the number of nodes, the total length of tubes, and total numbers of tube junctions, showed significant differences between the two groups (Fig. 4 (D)). Besides, the expression of HIF1A, VEGFA were increased (Fig. 4 (E)), indicating the positive role of HdECM in angiogenesis in vitro.

4. In vitro osteogenesis of HdECM

Under osteogenic induction culture, on day 7, compared to the empty control, hBMSCs treated with HdECM demonstrated an increase in ALP activity, as shown by the darker and denser blue-stained space in ALP staining and the ALP level kit's quantification analysis. On day 14, mineralized nodules stained by ARS demonstrated both a qualitative and significant quantitative increase in the HdECM-treated hBMSCs (Fig. 4 (F)). Osteogenic genes COL1A1, ALPL, RUNX2 and BGLAP were upregulated with the treatment of HdECM compared to the control, with the cytological results, further indicating HdECM promoted osteogenic differentiation of hBMSCs (Fig. 4 (G)).

5. 3D printing of hybrid scaffolds and their characterization

We developed a PCL/hydrogel hybrid scaffold for bone regeneration. The extraction using pepsinization to form either a solution or hydrogel was used extensively for decellularized tissues [35,36,42]. HdECM solution with a homogenously transparent appearance was obtained after a 48-h pepsin treatment. As described in the previous protocols [43] [–] [45], mild modification was attempted to form the hybrid gel, in which the soluble HdECM (10 mg/ml) was mixed with fibrinogen solution (10 mg/ml) and crosslinked with thrombin (100U/ml) at 10:10:1, followed by being poured into the pores of PCL scaffolds to generate the bone scaffold (Fig. 5 (A)). Scanning electron microscopy confirmed the hybridization of PCL-hydrogel structural composition (Fig. 5 (B)). The pores between PCL strands were filled with hydrogel networks, in which fibrin gel showed a network of small fibrin fibrils. In contrast, the fibrin/HdECM hybrid gel showed larger swelling bundles. The larger swelling bundles suggest that HdECM was interlocked within the fibrin network (Fig. 5 (B)). Taken all these, compared to the pure PCL (PP) scaffold, the PCL/fibrin (PF) scaffold, and the PCL/fibrin/HdECM (PFE) scaffold provided macro-to-micro interconnected pores that were compatible for cell adherence, migration, and proliferation.

6. Biocompatibility 3D-printed hybrid scaffolds

A CCK-8 assay was performed to determine the proliferation of hBMSCs on all scaffolds. The results showed that cells exhibited a positive proliferation on all scaffolds with the increase of the co-culture time, except a cessation of proliferation in the PF scaffold group on day 5, which might be attributed to cell confluence (Fig. 5 (C)). A significant increase in cell proliferation was observed in the PFE group, which suggested that the functionalization of PCL/fibrin with HdECM increase the scaffold biocompatibility. The live/dead staining assay on day 3 showed that few cells were dead (red) after being seeded, indicating that all scaffolds possessed good biocompatibility (Fig. 5 (D)). Live cells showing a normal spreading morphology were presented on all scaffolds. In particular, signs of cells were observed between the PCL strands in PF and PFE groups. The fibrin and fibrin/HdECM gel provided the additional space for cell adherence, migration. Together, PP, PF, and PFE scaffolds all possessed good biocompatibility and were beneficial for cell adherence, migration and proliferation.

7. The pro-angiogenic microenvironment of Fibrin/HdECM hybrid gels and 3D-printed PCL/fibrin/HdECM scaffold

The investigate the angiogenic ability of the hybrid gel systems, an ex vivo rat aortic ring sprouting angiogenesis assay was carried out. The median migration distance of cells was measured by placing the ring within the fibrin and fibrin/HdECM gel. A significant difference was observed on day 7 (Fig. 5 (E)). The LCSM images on day 7 qualitatively showed a greater abundance of sprouting cells and a denser branching network in the fibrin/HdECM group compared to the fibrin group. The ex vivo model suggested that the fibrin/HdECM gel provided a matrix beneficial for the out-migration of endothelial cells, leading to enhanced angiogenesis. To further evaluate the in vivo response, respective scaffolds were implanted in a rat subcutaneous pouch (Fig. 5 (F)). None of the scaffolds evoked a noticeable host inflammatory response. H&E images of the retrieved scaffolds after 7 and 31 days of implantation showed signs of tissue infiltration. However, a denser fibrous network and more populated cells were visible in PF and PFE than PP on day 7. The PF and PFE showed extensive microvascularity in both the short and long term. Moreover, erythrocytes observed within the microvessels indicated the integration of functional host vasculature. CD31 immunochemical staining was carried out to identify the perfused microvasculature. As depicted, the numbers of CD31 positive stains showed an ascending trend among three groups on both days 7 and 31 (Fig. 5 (G)). Quantification of microvessel density based on CD31 positive stains showed that PFE had a significant increase in host vascular infiltration than PF and PP in both the short and long term. Overall, these results indicated that both the fibrin gel and fibrin/HdECM gel were suitable beds for cell migration or sprouting. The addition of the angiogenic HdECM substrate into the fibrin gel further enhanced vascular infiltration from the host, indicating that the 3D-printed PCL/fibrin/HdECM hybrid scaffold could create a microenvironment promoting in situ angiogenesis.

8. The pro-osteogenic microenvironment of 3D-printed PCL/fibrin/HdECM scaffold

The osteogenic differentiation of hBMSCs on PP, PF, and PFE scaffolds was evaluated by ARS staining to determine the matrix mineralization. A more intense red staining (indicating calcium deposition) was observed in PF and PFE than in PP samples (Fig. 5 (H)). The PFE scaffolds showed the highest bone mineralization among other samples. Quantification of ARS showed a statistical significance among all groups (Fig. 5 (I)). The PFE yielded the highest production of calcium deposition, as indicated. Compared to the PP, both the PF and PFE, which had the fibrin and fibrin/HdECM gel incorporated into scaffold pores, provided additional space for cell adherence and infiltrative proliferation reasonable to provoke enhanced mineralization. However, with the addition of HdECM, PFE exhibited a significant increase compared to PF, which further verified that HdECM positively contributed to the osteogenesis of hBMSCs and the 3D-printed PCL/fibrin/HdECM could promote osteogenic differentiation.

9. BMSCs recruitment of 3D-printed PCL/fibrin/HdECM scaffolds

To investigate whether the PCL/fibrin/HdECM could be a microenvironment recruiting endogenous cells, a mimicking in vitro Transwell® assay was performed. The PFE scaffold demonstrated the properties of enhancing hBMSCs migration by 1.5-fold about the PP and PF (Fig. 5. (J,

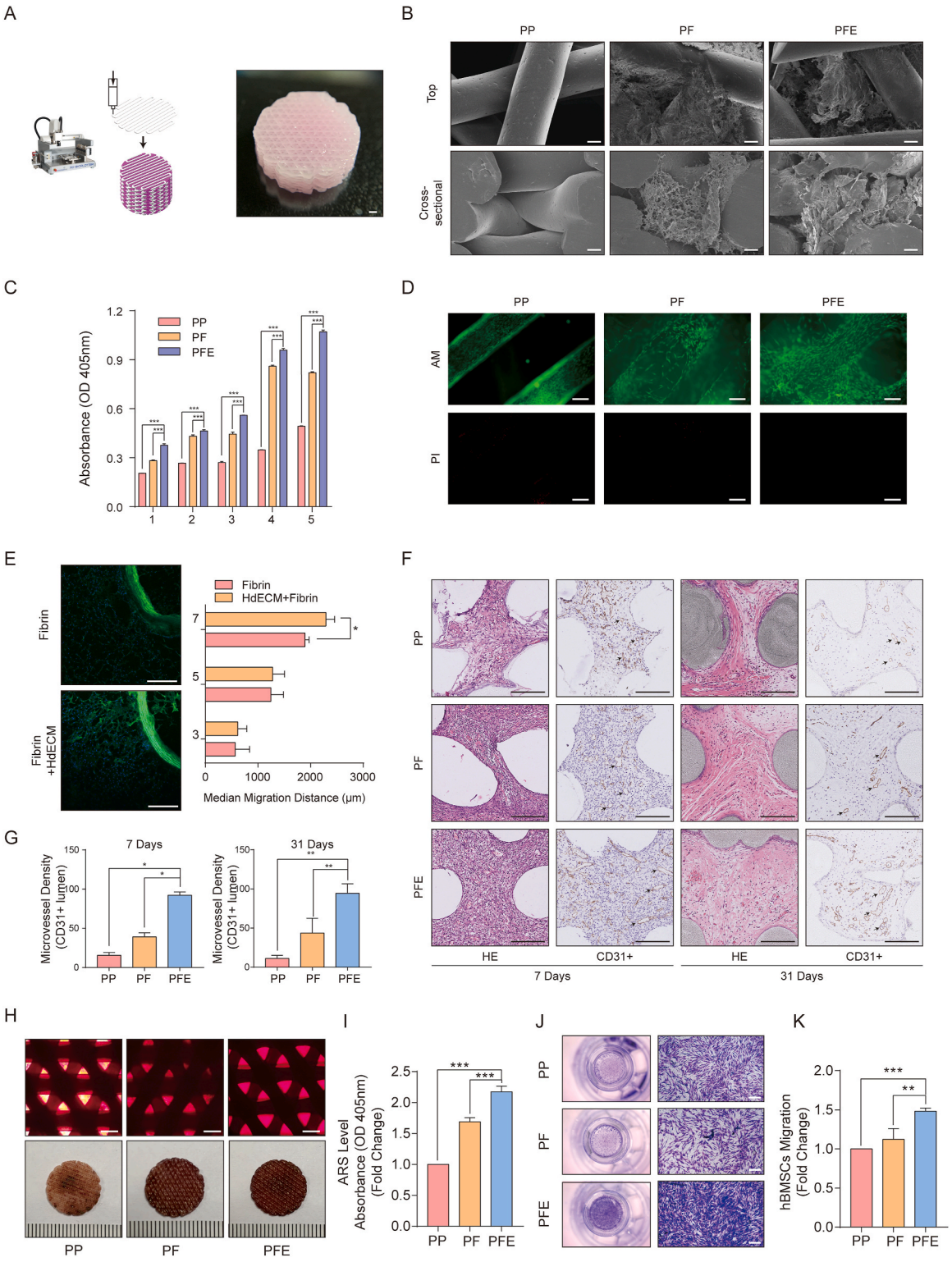

Fig. 5. Characterization of 3D-printed PCL/fibrin/HdECM scaffold and its effect on angiogenesis and osteogenesis. **A,** Schematic demonstration of dual-head printing using 3D-bioplotter to fabricate the PCL/fibrin/HdECM hybrid scaffold, and its gross view (phenol red) was added HdECM/fibrin solution for better visualization). Scale bar = 1 mm. **B,** Representative images of scanning electron microscopy showing the cross-sectional and top view of the scaffolds of pure PCL scaffold (PP), PCL/fibrin scaffold (PF), PCL/fibrin/HdECM scaffold (PFE). Scale bars = 100 μm. **C,** CCK-8 assay shows cell toxicity and proliferation after culturing with different scaffolds for consecutive 5 days. **D,** Live/dead assay showing cell viability after culturing hBMSCs on scaffolds for 72 h. Live cells appeared green, whereas dead cells appeared red. E, Representative images and quantification of rat aortic ring assay to evaluate the ex vivo angiogenic capacity fibrin gel or fibrin/HdECM gel. **F,** Histology of hybrid scaffolds after subcutaneous implantation for 7 and 30 days, respectively. Arrow: CD31 positive lumen. **G,** Quantification of $CD31^{+}$ micro-vessels in the subcutaneous implantation model. **H,** Representative images of ARS staining hybrid scaffolds seeded with hBMSC under osteoinductive culture condition for 14 days. **I,** Quantification of ARS of osteogenic hBMSC seeded on hybrid scaffolds. **J,** Chemotaxis assay of hybrid scaffolds. * Significant difference, $P < 0.05$; ** Very significant difference, $P < 0.01$; *** Highly significant difference, $P < 0.001$. (For interpretation of the references to color in this figure legend, the reader is referred to the Web version of this article.)

K)).

10. In vivo bone regeneration and osseointegration of 3D-printed PCL/fibrin/HdECM scaffolds

Based on the in vitro studies, all scaffolds were implanted into a rat femoral epicondylar bone defect model to investigate theirs in vivo functionality of osteogenesis. No postoperative complications such as infection or death were observed among all rats. The punched scaffold matched the cylindrical defect as desired. The region of interest (ROI) was depicted, which the outer and inner circle/triangle represented the general scaffold and its most central region (Fig. 6 (A)). The two-dimensional μ-CT images were obtained, revealing that bone grew from the scaffold periphery to its central region and filled the pore space which was initially occupied by the fibrin gel and fibrin/HdECM gel (Fig. 6 (B)). Minimal bone ingrowth was observed in the sham control. Various degree of bone ingrowth was present among 3D-printed scaffolds, with most condensed bone quality in PFE scaffolds. The radiolucent patterns represented the structs of PCL scaffolds, along with the ingrowth of bone tissue suggested that 3D-printed scaffolds allowed tissue ingrowth within their interconnected pores. Three-dimensional reconstructed images further verified the bone ingrowth (Fig. 6. (C, E)). PFE had the most bone ingrowth in quantity among all others in both 2- and 4-weeks post-implantation. Besides, at 4 weeks, reconstructed images demonstrated a thicker bone structure between PCL struts in PFE scaffolds. PFE scaffolds showed a significant bone mass compared to sham, PP, and PF with regard to the central region. Quantitative analysis of BV/TV revealed a significant ascending trend of bone regeneration among all groups in terms of either the general or internal region, among which PFE scaffolds were of the best (Fig. 6. (D, F)). These indicated that PFE enhanced osseointegration in a time-dependent manner. The histological analysis further revealed the possible mechanism related to the phenomenon. The samples' representative images at 2 and 4 weeks after implantation were shown (Fig. 7. (A, B)). In H&E and Masson-stained sections, the struts of scaffolds, fibrous connective tissue, and bone were present. No obvious inflammatory host reaction was observed among all groups. A greater proportion of fibrous connective tissue ingrowth was shown within the central region of sham controls or 3D-printed scaffolds, along with a minor degree of new bone formation. In the sham group, loose connective tissues were present within the defect accompanied by bone migration signs from the periphery at both timepoints. At 2 weeks, only a few traits of unmineralized bone matrix were observed in PP scaffolds. However, new mineralized bone was presented in PF and PFE scaffolds, with better quality and quantity in the later samples. At 4 weeks, both the sham and PP scaffolds remained largely infiltrated by connective fibrous tissues or unmineralized matrices. PF scaffolds had an increase of bone ingrowth though the central region remained occupied by fibrous tissues. However, PFE scaffolds exhibited optimal bone ingrowth showing signs of mature new bone and reconstruction of bone marrow sinuses. In PFE scaffolds, compared to the images at 2 weeks which PCL structs were encapsulated with a thin layer of fibrous tissues, bone or bone marrow was directly in contact with structs. This observation was consistent with a thicker bone structure between PCL struts in PFE on μ-CT scanning. The histological results confirmed the microenvironment created by the PFE scaffolds mediated superior bone ingrowth and osseointegration.

11. Neovascularization of 3D-printed PCL/fibrin/HdECM scaffolds

To study whether bone regeneration was related to neovascularization mediated by the scaffold, vessel formation of all groups after 2 weeks of epicondylar implantation was studies using angiographic μ-CT imaging. Digital reconstructed angiographic images were displayed (Fig. 6. G). All groups showed a certain degree of vessel discontinuity, indicating that the femoral defect created by a drill disrupted the vascular network along with bone loss. Compared to sham, PP and PF groups with 2–3 perfused vessels surrounding the defect area, PFE demonstrated a densely perfused vascular network, suggesting the scaffold promoted the vascular anastomoses from the adjacent tissue. Similar to the presentation of new bone ingrowth, vascular infiltration was present within the central region in the PFE scaffolds. Statistical significance ($P < 0.05$, $n = 3$) was found in the PFE group in terms of vascular volume.

12. A local microenvironment coupling angiogenesis (type-H vessels) and osteogenesis (osterix^{+} progenitors) through activating HIF-1A pathway of 3D-printed PCL/fibrin/HdECM scaffold

To investigate whether the coupled angiogenesis and osteogenesis were related to type H vessel formation, CD31, endomucin, and osterix immunostaining were performed on bone sections after 2 weeks of implantation. Within the central region of PFE group, CD31^{+}Endomucin^{+} signals were observed. In contrast, only CD31^{+} signals were present in sham, PF and PFE groups (Fig. 8. A). Quantification of endomucin fluorescent intensity further confirmed a significant ($P < 0.05$) upregulated state of type H vessels in the PFE mediated microenvironment (Fig. 8. D). Besides, osterix + osteoprogenitors were the highest in the PFE group (Fig. 8. (A, D)). These indicated that the PFE scaffold mediated a bio-instructive microenvironment for endogenous cells to achieve coupled angiogenesis and osteogenesis. Furthermore, HIF-1A immunostaining and intensity quantification (Fig. 8. (C, D)) demonstrated that the increased expression of the newly formed tissue, indicating the coupled angiogenesis and osteogenesis, was possibly related to the activation of HIF-1A pathway.

4. Discussion

The local microenvironment in diseased or traumatized bone is usually altered or compromised, manifesting as the impaired formation of blood vessels and new bone due to a disruption of coupled angiogenesis and osteogenesis [30,46]. The reciprocal relationship of neovascularization and bone regeneration is regulated by complex crosstalk between endothelial cells and osteoprogenitors [9,30,47–56]. In response to chemoattractants, ECs and osteoprogenitors are recruited by direct migration from their niches or defect edges and then proliferate and differentiate into vessels and bone [57]. Recently, along with the expanding knowledge on cellular mechanism between bone-specific ECs and osteoblasts, a subtype of bone capillaries coupling osteogenesis, namely type H vessels, was characterized. Type H vessels were defined by high expression of CD31 and Endomucin (CD31^{h}iEndomucin^{hi}), were densely surrounded by osteoblastic progenitors expressing Osterix. Anatomically, flows of oxygen-rich blood reach type H vessels directly from arteries and distal arterioles. Their proximity to osteoprogenitors give rise to the osteoblasts for bone formation, while the high oxygen content in type H vessels supplies nutrients for host bone ingrowth. Additionally, by producing factors such as VEGF and Notch that stimulate proliferation and differentiation of bone marrow-derived osteoprogenitors, type H vessels are angiogenic vessels forming the leading tip of capillaries growth in the bone and direct bone regeneration [30,31,51,56,58].

Our findings verified the hypothesis that the bio-instructive microenvironment, employing the angiogenesis and osteogenesis functionality of HdECM, had achieved early vascular infiltration and rapid bone mineralization in situ, as revealed by type H vessel formation, activation of HIF-1α signaling and accelerated bone mineralization. In our study, μ-CT showed that new bone infiltrated the PFE scaffold from the periphery to the central region, and μ-AG depicted a dense anastomosis of a vascular network within the scaffold (Fig. 6. (G, H)). The immunofluorescent images of the implanted PFE scaffold demonstrated a significant increase of CD31^{hi}Emdomucin^{hi} lumen-like structures, particularly in the newly formed bone located in the central region (Fig. 8. (A, D)). As

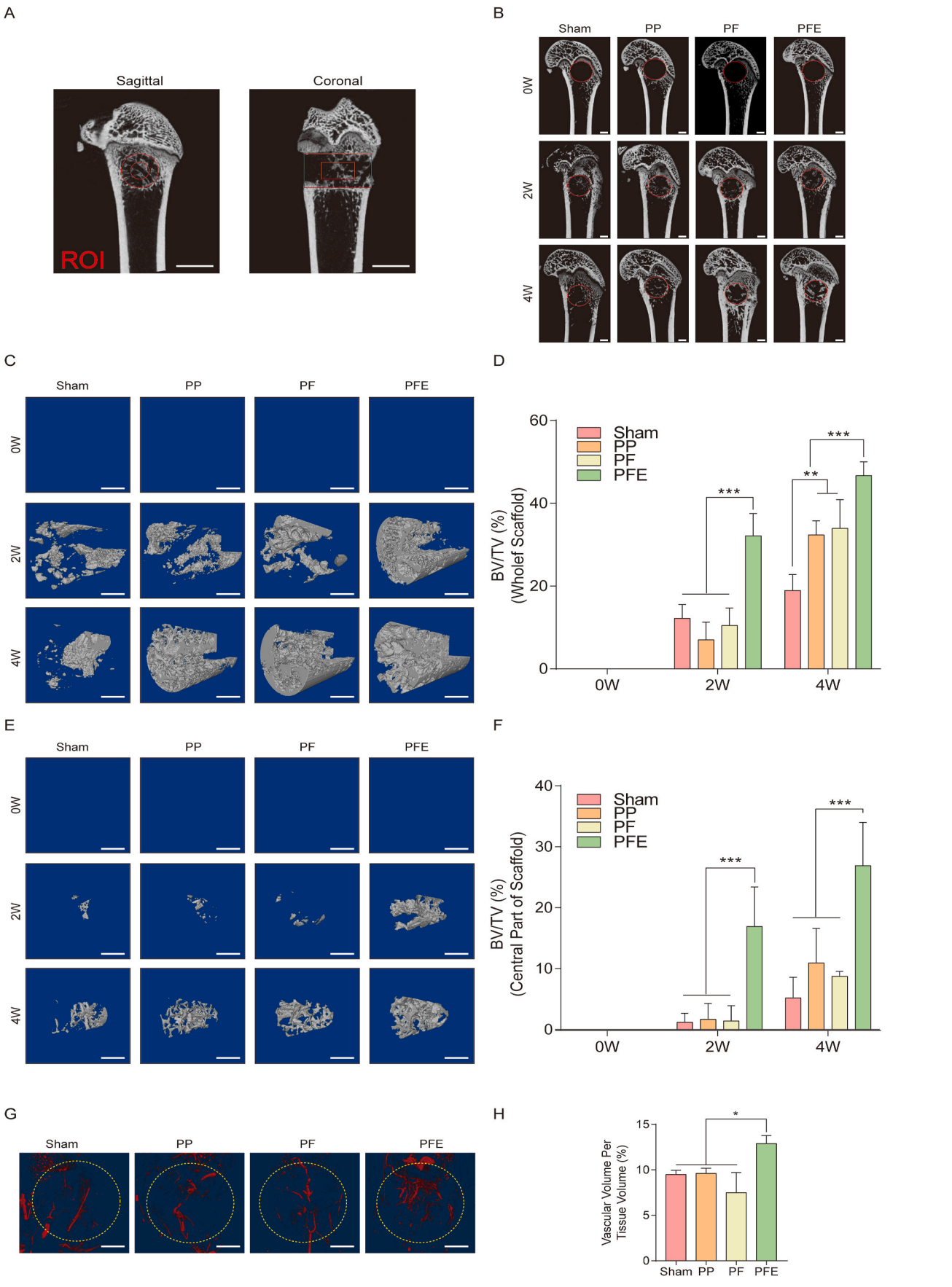

(caption on next page)

Fig. 6. Evaluation of bone regeneration of 3D-printed PCL/fibrin/HdECM scaffold and controls after rat femoral epicondyle implantation. (n = 4). **A,** Images depict the region of interest (ROI). The outer circle and rectangle depict the general contour of hybrid scaffolds, while the inner circle and rectangle illustrate the central region. **B,** Representative images of micro-CT reconstruction of the newly formed bone in sham, PP, PF, and PFE. **C,** Representative images of 3D reconstruction of the newly formed bone within the bone defect (D: 3 mm, H: 5 mm). **D,** Quantification of BV/TV based on C. **E,** Representative images of 3D reconstruction of the newly formed bone within the central region (D: 1.5 mm, H: 2.5 mm) of the bone defects (sham) and scaffolds (PP, PF, PFE). **F,** Quantification of BV/TV of the central region of the bone defects (sham) and scaffolds (PP, PF, PFE). **G,** Representative images of 3D-reconstructed microvessel distribution in the defect area. **H,** Quantification of microvessel density in the defect area. Abbreviations: Pure PCL, PP; PCL/fibrin, PF; PCL/fibrin/HdECM, PFE; Bone volume/tissue volume, BV/TV; Diameter, D; Height, H. * Significant difference, $P < 0.05$; ** Very significant difference, $P < 0.01$; *** Highly significant difference, $P < 0.001$.

reported by the preceding works of literature, Osterix^{+} osteoprogenitors densely infiltrated within the scaffold (Fig. 8. (B, D)). Previous gain/loss-of-function studies have revealed that the activation of hypoxia signaling in ECs could lead to an increased formation of type H vessels and enhanced coupled angiogenesis and osteogenesis [30,31,59]. Our results demonstrated the increased expression of HIF-1A mediated by the PFE scaffold (Fig. 8. (C, D)), which agrees with the earlier results on the associated role of HIF-1A and type H vessel formation.

As mentioned earlier, one of the concerns hindering the broad translation of bio-inert polymer scaffold as bone substitute is due to the suboptimal biological interactions with cells in vitro and fibrous encapsulation upon in vivo implantation [60]. Traditionally, different methods have been utilized, such as surface coating or modification, incorporating bioactive ingredients, to attempt improved osseointegration [10,11,13,60]. These methods possessed respective drawbacks, including osteolysis caused by debris desquamating from the surface, host immune rejection, adverse reactions led by super-physiological delivery of growth factors [2,13,16,17,20,61]. Methods developed from the viewpoint of increasing bioactivity in vitro and in vivo overlooked the possibility that the creation of microenvironments might potentiate the osseointegration process by inducing the formation of type H capillaries. A previous study fabricated a PCL-based biomimetic tissue-engineered periosteum (TEP) and observed the induction of distinct type H vessels and marked osseointegration [62]. It suggested that early type H vessel induction could have led to improved osseointegration. Consistently, we demonstrated that the rapid type H vessels related-neovascularization mediated by the PFE microenvironment had counteracted the bio-inertness of PCL polymer, leading to superior osseointegration. In μ-CT scanning, the newly formed bone in PFE scaffolds exhibited a thicker pattern between PCL struts than the PP and PFE groups. Histologically, PCL struts of the PF scaffolds were encapsulated by connective fibrous tissue in both 2 and 4 weeks, while struts of the PFE scaffold were in direct contact with the newly formed bone and marrow cavities in 4 weeks, indicating marked improvement of osseointegration (Fig. 6.). Previous studies have shown that reactivation of type H vessels led to new bone formation and hematopoiesis [30,51], which was also observed in the PFE group in which bone marrow cells were infiltrated. The PFE scaffold, demonstrating a direct hard tissue bonding and restoration of bone marrow, had achieved a successful biointegration [63]. Hence, these findings suggested that type H vessel-targeted biofabrication might also be applied in other polymeric bone substitutes such as polyetheretherketone (PEEK) or polylactic acid (PLA), allowing for optimal osseointegration and biontegration.

Extracellular matrix (ECM) is a nature-designed biomaterial that underwent material optimization for over 600 million years [64]. Decellularized ECM (dECM) is composed of a complex assembly of proteins, glycosaminoglycans (GAGs), and growth factors, whose role on tissue regeneration has been a hot topic for the past decade [21,22,24–27,35,42,65–73]. To recapitulate the regenerative bone microenvironment, cell-derived decellularized extracellular matrix (CD-dECM), whose specific composition varies from cell to cell, including MSC, fibroblasts, and osteoblasts, has been adopted as a cell-instructive biomaterial for bone regeneration, considering it as a reservoir of multiple growth factors and cytokines and play a pivotal role in cell adhesion, differentiation, and proliferation [22,28,35,66,73–75]. A large body of evidence has demonstrated that endothelial cell (EC) derived extracellular matrix regulates cell migration, proliferation and provides guidance cues supporting capillary morphogenesis through various signaling pathways [26,27,29,55,76]. Besides, previous research has demonstrated that CD-dECM derived from human umbilical vein endothelial cells (HUVECs) has shown respective osteogenic and angiogenic capacity in vitro, from cell to molecular levels, whereas in vivo studies lacked [23–26,61].

Several biological events and functions were implicated in our proteomic analysis. HdECM comprises different proteins such as laminin, collagen and fibronectin, whose roles such as protein and growth factors binding, cell adhesion, cell proliferation and differentiation have been previously studied [77]. The multiple functions of HdECM were verified by our GO enrichment analysis. Of note, proteins within HdECM were related to osteoblast and endothelial differentiation, consistent with the evidence as mentioned above (Fig. 3.). Our group also proved that HdECM could preserve its angiogenic and osteogenic functionality after the pepsin solubilization treatment (Fig. 4.), a widely used method in fabricating ECM gel or bio-inks. hBMSCs exhibited enhanced osteogenic differentiation at 7- and 14-day periods with the supplementation of solubilized HdECM (Fig. 4. (F, G)). Although proliferation assay revealed insignificant results on HUVECs, significant results in the migration and tube formation assay were observed and consistent with previous evidence on its role in EC morphogenesis (Fig. 4. (B, C, D, E)). Then, solubilized HdECM crosslinked within fibrin gel was further incorporated into the pores of the PCL scaffold to engineer a bio-instructive microenvironment for in vivo experiments. The in vivo implantation of a rat femoral epicondylar bone defect model revealed that the scaffold successfully mediated the respective endothelial and osteoblastic differentiation of endogenous cells to achieve in situ vascularized bone regeneration. The 3D-printed PCL/fibrin/HdECM hybrid scaffold capable of recruiting endogenous cells, as confirmed both in vitro and in vivo, provided a scaffold-mediated angiogenic and osteogenic microenvironment (Figs. 4–6). Within the softer infill of fibrin/HdECM gel distributed in the interconnected pores of the robust PCL framework, endogenous ECs were capable of migrating and sprouting to generate a new perfused vascular network (Fig. 5. (E, H)). At the same time, endogenous osteoblasts were guided to lay down bone minerals. Our μ-CT and histological results demonstrated a greater bone mass within PFE scaffolds than controls, and the lumens or cavities within the newly formed bone contained red blood cells (Figs. 6 and 7.). These suggested that the PFE microenvironment facilitated early functional neovascularization and host bone infiltration compared to the PF, PP, and sham. Conventionally, recombinant GFs such as BMP and VEGF were used in combination with polymeric scaffold but failed to recapitulate the complexity of crosstalk between angiogenesis and osteogenesis, which ectopic bone and malformed vasculature presented adversely [8,16,19,39,61,78,79]. Compared to the recombinant GFs, HdECM was proved to mediate the crosstalk of angiogenesis and osteogenesis, convenient in obtainment, minimally immunogenic, and biologically safer. It constitutes an ideal complex of biomolecular cues within a physiological combination and dosage that could recapitulate a bio-instructive microenvironment.

Polycaprolactone (PCL), approved by the Food and Drug Administration (FDA), has been used for 3D printing and demonstrated considerable mechanical robustness and controlled porosity in preclinical and clinical studies. Our previous study has fabricated a PCL framework with interconnected macropores around 300 μm as mechanical support, exhibited feasibility for bone ingrowth and vasculature remodeling

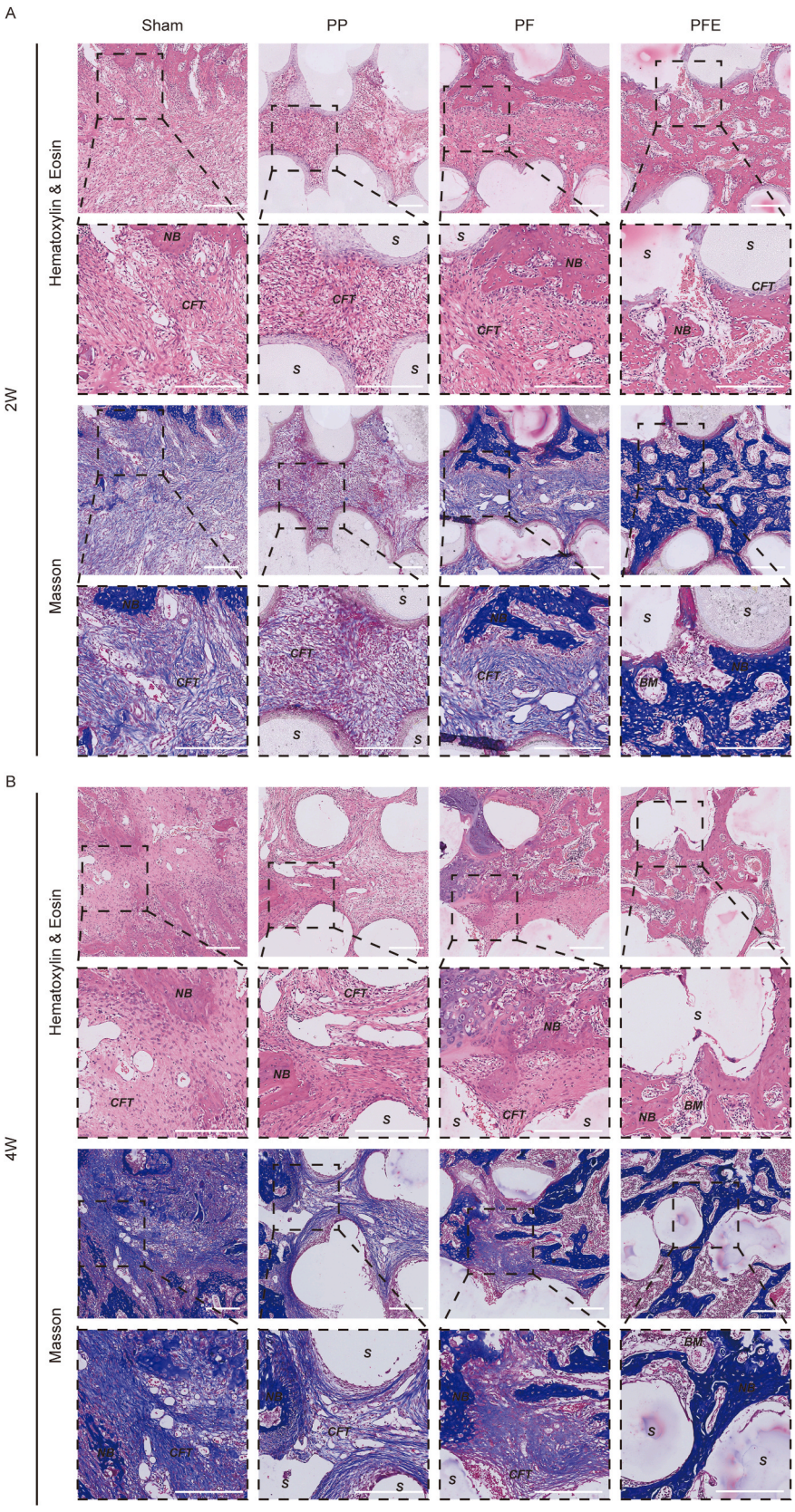

Fig. 7. Histology of bone regeneration of 3D-printed PCL/fibrin/HdECM scaffold and controls in vivo. **A,** Representative H&E and Masson staining images of the central region of the implanted scaffold at 2 weeks. Scale bar = 250 μm **B,** Representative H&E and Masson staining images of the central region of the implanted scaffold at 4 weeks. Scale bar = 250 μm. Abbreviations: NB, new bone; CFT, connective fibrous tissue; BM, bone marrow; S, scaffold.

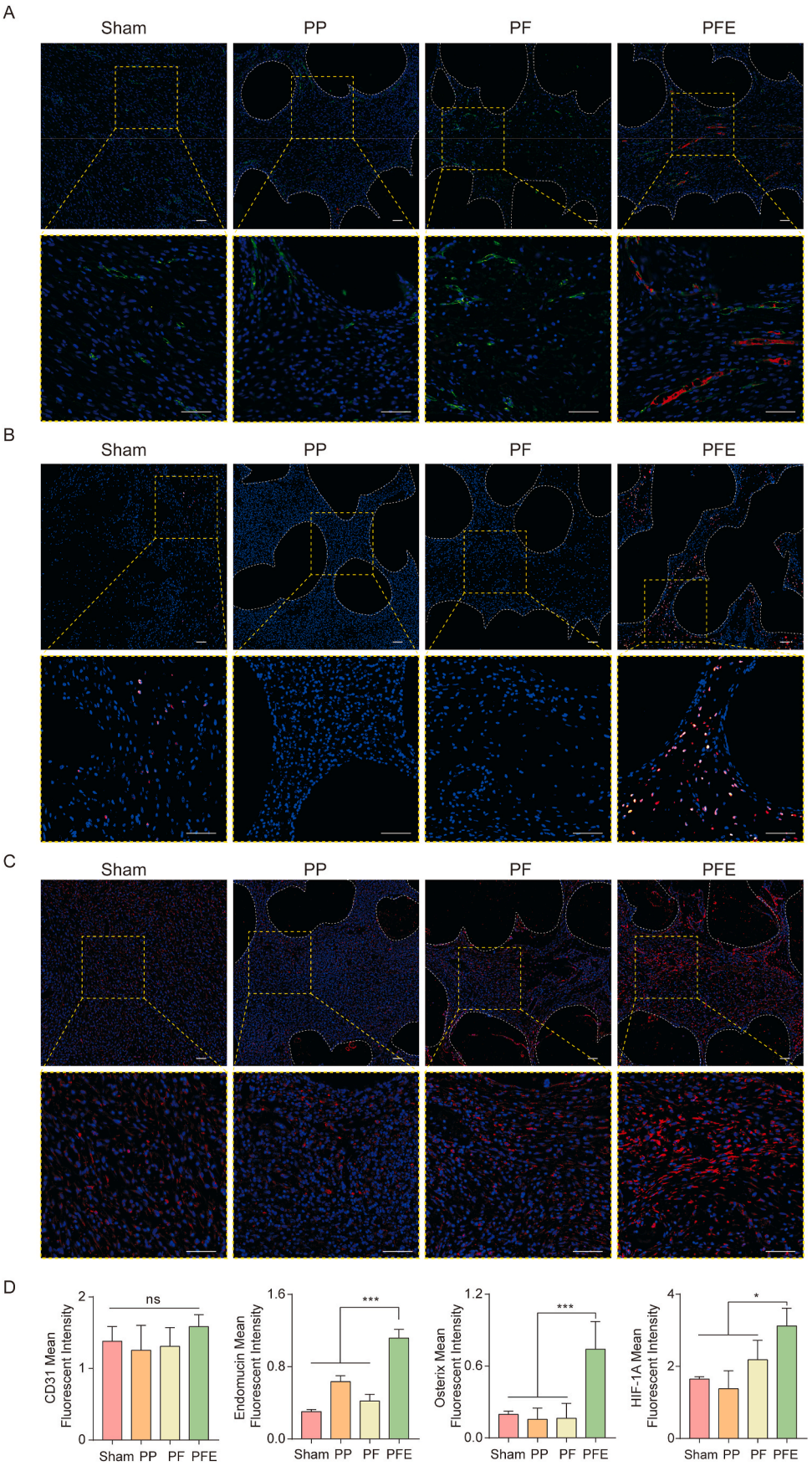

Fig. 8. Immunofluorescence of type-H vessels (Endomucin$^+$ & CD31$^+$), osteoprogenitor cells (Osterix$^+$) and HIF-1α. **A,** Representative immunofluorescent images of type-H vessels in the central region of scaffolds. Endomucin$^+$, red; CD31$^+$, green; DAPI, blue. **B,** Representative immunofluorescent images of Osterix$^+$ osteoprogenitor cells in the central region of scaffolds. Osterix$^+$, red; DAPI, blue. **C,** Representative immunofluorescent images of HIF-1α$^+$ cells in the central region of scaffolds. HIF-1α$^+$, red; DAPI, blue. Scale bar = 50 μm. **D,** Quantative analysis of fluorescent intensity of CD31, Endomucin, Osterix and HIF-1A expression, respectively. * Significant difference, $P < 0.05$; ** Very significant difference, $P < 0.01$; *** Highly significant difference, $P < 0.001$. (For interpretation of the references to color in this figure legend, the reader is referred to the Web version of this article.)

[80]. Taking a hybrid strategy, we intended to improve the bio-activeness and minimize the fibrous encapsulation PCL using the fibrin or HdECM/fibrin hydrogel, which 'insulated' the scaffold with a bio-instructive microenvironment. By infilling the gel with a custom-made device, both fibrin and fibrin/HdECM gel could be incorporated within PCL scaffolds and exhibited a macro-to-micro porous structure under SEM (Fig. 5 (B)). Evidence has been accumulated that such structure allowed the internal migration, sprouting of cells and achieved superior osseointegration [81], as demonstrated in our result. Fibrin is a derivative constituent of hematoma involved in the initial healing phase of bone defect, a natural matrix preamble for nutrient and oxygen transportation, host cell infiltration, and tissue regeneration [82]. HdECM that crosslinked within the fibrin provided additional cues for both endothelial cells' migration and sprouting and MSCs' proliferation and differentiation as revealed (Fig. 5. (C - I)). The hybrid fabrication method by infilling the "hard" polymer framework with the "soft" hydrogel that targeted the formation of type H vessels might also be applied in other polymeric bone substitutes as synthetic polymers widely share hydrophobicity and bio-inertness and demonstrated fibrous encapsulation after implantation to some degree.

Our study has some limitations. Although the solubilization of CD-dECM using pepsin was generally used [35,36,70], the treatment would cause some degree of alteration in both physical structure and biochemical composition. The alteration during the process had not been thoroughly studied and discussed. Furthermore, the formation of type H vessels was related to multiple mechanisms involving different growth factors and molecules. Due to the complexity of biomolecules contained within HdECM and the effect that appeared multifaceted, we could not study the exact mechanism on how HdECM affects the formation of type H vessels. To further investigate the questions, in-depth analysis to clarify the exact biomolecules and related signaling pathways should be performed in the future.

5. Conclusion

Utilizing the biomolecular properties of HdECM, we successfully fabricate a PCL/fibrin/HdECM hybrid scaffold. The acellular scaffold recruits the endogenous cells to support their angiogenic and osteogenic differentiation, showing evidence of the generation of type H vessels and activation of HIF-1α. Besides, HdECM possesses the unique combination of biomolecules essential in the crosstalk between ECs and OPs, as well as mimics a bio-instructive microenvironment for coupled angiogenesis and osteogenesis but carries less immunogenicity and adverse effects than recombinant GFs. The concurrent presence of type H vessels and diminished fibrous encapsulation of PCL scaffolds might provide a clue for future research that type H vessel-targeted biomaterials could improve osseointegration. The present hybrid scaffold successfully achieves superior osseointegration as well as rapid vascularized bone regeneration. All these have demonstrated the possible value in future translation.

Author contributions

The manuscript was written through the contributions of all authors. All authors have approved the final version of the manuscript. *These authors contributed equally.

CRediT authorship contribution statement

Yijun He: Conceptualization, Data curation, Formal analysis, Investigation, Methodology, Validation, Visualization, Writing – original draft, Writing – review & editing. **Wenhao Wang:** Conceptualization, Funding acquisition, Validation, Visualization, Writing – review & editing. **Shaozhang Lin:** Investigation, Methodology, Validation, Visualization. **Yixi Yang:** Investigation, Methodology. **Lizhi Song:** Investigation, Methodology. **Yihan Jing:** Investigation, Methodology. **Lihao Chen:** Investigation, Methodology. **Zaopeng He:** Funding acquisition, Resources, Software, Validation. **Wei Li:** Funding acquisition, Resources, Software, Validation. **Ao Xiong:** Conceptualization, Methodology. **Kelvin W.K. Yeung:** Conceptualization, Methodology. **Qi Zhao:** Resources, Software. **Yuan Jiang:** Resources, Software. **Zijie Li:** Resources, Software. **Guoxian Pei:** Conceptualization, Supervision, Funding acquisition. **Zhi-Yong Zhang:** Conceptualization, Supervision, Funding acquisition.

Declaration of competing interest

The authors declare that we have no financial and personal relationships with other people or organizations that can inappropriately influence our work, there is no professional or other personal interest of any nature or kind in any product, service and/or company that could be construed as influencing the position presented in the manuscript entitled "Fabrication of a bio-instructive scaffold conferred with a microenvironment allowing for superior implant osseointegration and accelerated in situ vascularized bone regeneration via type H vessel formation".

Acknowledgments

This work was supported by the National Natural Science Foundation of China (NSFC) (Nos. 82072415, 81772354, 81902189), Clinical Innovation Research Program of Guangzhou Regenerative Medicine and Health Guangdong Laboratory (2018GZR0201001), Science Technology Project of Guangzhou City (2019ZD15), Collegiate Innovation and Entrepreneurship Education Project of Guangzhou City (2019PT104), Science and Technology Innovation Project of Foshan City (1920001000025), and National Young Thousand-Talent Scheme to Zhang Zhi-Yong.

Appendix A. Supplementary data

Supplementary data to this article can be found online at https://doi.org/10.1016/j.bioactmat.2021.07.030.

References

[1] C. Mauffrey, B.T. Barlow, W. Smith, Management of segmental bone defects, J Am Acad Orthop Sur 23 (2015) 143–153, https://doi.org/10.5435/jaaos-d-14-00018r1.
[2] W. Wang, K.W.K. Yeung, Bone grafts and biomaterials substitutes for bone defect repair: a review, Bioact Mater 2 (2017) 224–247, https://doi.org/10.1016/j.bioactmat.2017.05.007.
[3] J.S. Lee, Y. Jin, H. Park, K. Yang, M.S. Lee, H.S. Yang, S. Cho, In situ bone tissue engineering with an endogenous stem cell mobilizer and osteoinductive nanofibrous polymeric scaffolds, Biotechnol. J. 12 (2017) 1700062, https://doi.org/10.1002/biot.201700062.
[4] J.J. Rice, M.M. Martino, L.D. Laporte, F. Tortelli, P.S. Briquez, J.A. Hubbell, Engineering the regenerative microenvironment with biomaterials, Adv Healthc Mater 2 (2013) 57–71, https://doi.org/10.1002/adhm.201200197.
[5] M.N. Collins, G. Ren, K. Young, S. Pina, R.L. Reis, J.M. Oliveira, Scaffold fabrication technologies and structure/function properties in bone tissue engineering, Adv. Funct. Mater. (2021), https://doi.org/10.1002/adfm.202010609.
[6] J. Shen, W. Wang, X. Zhai, B. Chen, W. Qiao, W. Li, P. Li, Y. Zhao, Y. Meng, S. Qian, X. Liu, P.K. Chu, K.W.K. Yeung, 3D-printed nanocomposite scaffolds with tunable magnesium ionic microenvironment induce in situ bone tissue regeneration, Appl Mater Today 16 (2019) 493–507, https://doi.org/10.1016/j.apmt.2019.07.012.
[7] J.S. Miller, K.R. Stevens, M.T. Yang, B.M. Baker, D.-H.T. Nguyen, D.M. Cohen, E. Toro, A.A. Chen, P.A. Galie, X. Yu, R. Chaturvedi, S.N. Bhatia, C.S. Chen, Rapid casting of patterned vascular networks for perfusable engineered three-dimensional tissues, Nat. Mater. 11 (2012) 768–774, https://doi.org/10.1038/nmat3357.
[8] F. Shahabipour, N. Ashammakhi, R.K. Oskuee, S. Bonakdar, T. Hoffman, M. A. Shokrgozar, A. Khademhosseini, Key components of engineering vascularized three-dimensional bioprinted bone constructs, Transl. Res. 216 (2019) 57–76, https://doi.org/10.1016/j.trsl.2019.08.010.
[9] B.& J.R.G. K Centre for Human Development, Stem cells and regeneration, developmental origins of Health and disease, institute of developmental sciences, university of southampton, southampton, SO16 6YD, U., J. Kanczler, R. Oreffo,

osteogenesis and angiogenesis: the potential for engineering bone, Eur. Cell. Mater. 15 (2008) 100–114, https://doi.org/10.22203/ecm.v015a08.
[10] W. Wang, K.W.K. Yeung, Plasma surface modifications of orthopaedic biomaterials by the adoption of bioinorganic cations: a review, Surf Innov 8 (2019) 1–12, https://doi.org/10.1680/jsuin.19.00048.
[11] H. Chen, Q. Han, C. Wang, Y. Liu, B. Chen, J. Wang, Porous scaffold design for additive manufacturing in orthopedics: a review, Front Bioeng Biotechnol 8 (2020) 609, https://doi.org/10.3389/fbioe.2020.00609.
[12] X. Han, M. Sun, B. Chen, Q. Saiding, J. Zhang, H. Song, L. Deng, P. Wang, W. Gong, W. Cui, Lotus seedpod-inspired internal vascularized 3D printed scaffold for bone tissue repair, Bioact Mater 6 (2021) 1639–1652, https://doi.org/10.1016/j.bioactmat.2020.11.019.
[13] Y. Yan, H. Chen, H. Zhang, C. Guo, K. Yang, K. Chen, R. Cheng, N. Qian, N. Sandler, Y.S. Zhang, H. Shen, J. Qi, W. Cui, L. Deng, Vascularized 3D printed scaffolds for promoting bone regeneration, Biomaterials 190 (2019) 97–110, https://doi.org/10.1016/j.biomaterials.2018.10.033.
[14] R.C. de A.G. Mota, E.O. da Silva, F.F. de Lima, L.R. de Menezes, A.C.S. Thiele, 3D printed scaffolds as a new perspective for bone tissue regeneration: literature review, Mater. Sci. Appl. (2016) 430–452, https://doi.org/10.4236/msa.2016.78039, 07.
[15] S.F. Badylak, A scaffold immune microenvironment, Science 352 (2016), https://doi.org/10.1126/science.aaf7587, 298–298.
[16] X. Shen, Y. Zhang, Y. Gu, Y. Xu, Y. Liu, B. Li, L. Chen, Sequential and sustained release of SDF-1 and BMP-2 from silk fibroin-nanohydroxyapatite scaffold for the enhancement of bone regeneration, Biomaterials 106 (2016) 205–216, https://doi.org/10.1016/j.biomaterials.2016.08.023.
[17] A. Cipitria, J.C. Reichert, D.R. Epari, S. Saifzadeh, A. Berner, H. Schell, M. Mehta, M.A. Schuetz, G.N. Duda, D.W. Hutmacher, Polycaprolactone scaffold and reduced rhBMP-7 dose for the regeneration of critical-sized defects in sheep tibiae, Biomaterials 34 (2013) 9960–9968, https://doi.org/10.1016/j.biomaterials.2013.09.011.
[18] H.A. Rather, D. Jhala, R. Vasita, Dual functional approaches for osteogenesis coupled angiogenesis in bone tissue engineering, Mater. Sci. Eng. C 103 (2019) 109761, https://doi.org/10.1016/j.msec.2019.109761.
[19] W. Tang, Y. Yu, J. Wang, H. Liu, H. Pan, G. Wang, C. Liu, Enhancement and orchestration of osteogenesis and angiogenesis by a dual-modular design of growth factors delivery scaffolds and 26SCS decoration, Biomaterials 232 (2020) 119645, https://doi.org/10.1016/j.biomaterials.2019.119645.
[20] O.P. Gautschi, S.P. Frey, R. Zellweger, Bone morphogenetic proteins IN clinical applications, ANZ J. Surg. 77 (2007) 626–631, https://doi.org/10.1111/j.1445-2197.2007.04175.x.
[21] B.S. Kim, S. Das, J. Jang, D.-W. Cho, Decellularized extracellular matrix-based bioinks for engineering tissue- and organ-specific microenvironments, Chem. Rev. 120 (2020) 10608–10661, https://doi.org/10.1021/acs.chemrev.9b00808.
[22] K.P. Robb, A. Shridhar, L.E. Flynn, Decellularized matrices as cell-instructive scaffolds to guide tissue-specific regeneration, ACS Biomater. Sci. Eng. 4 (2017) 3627–3643, https://doi.org/10.1021/acsbiomaterials.7b00619.
[23] F.M. Lampert, F. Simunovic, G. Finkenzeller, D. Pfeifer, G.B. Stark, O. Winninger, D. Steiner, Transcriptomic changes in osteoblasts following endothelial cell-cocultivation suggest a role of extracellular matrix in cellular interaction, J. Cell. Biochem. 117 (2016) 1869–1879, https://doi.org/10.1002/jcb.25486.
[24] Y. Kang, S. Kim, J. Bishop, A. Khademhosseini, Y. Yang, The osteogenic differentiation of human bone marrow MSCs on HUVEC-derived ECM and β-TCP scaffold, Biomaterials 33 (2012) 6998–7007, https://doi.org/10.1016/j.biomaterials.2012.06.061.
[25] M.S. Carvalho, J.C. Silva, J.M.S. Cabral, C.L. Silva, D. Vashishth, Cultured cell-derived extracellular matrices to enhance the osteogenic differentiation and angiogenic properties of human mesenchymal stem/stromal cells, J Tissue Eng Regen M 13 (2019) 1544–1558, https://doi.org/10.1002/term.2907.
[26] T. Gong, B.C. Heng, J. Xu, S. Zhu, C. Yuan, E.C.M. Lo, C. Zhang, Decellularized extracellular matrix of human umbilical vein endothelial cells promotes endothelial differentiation of stem cells from exfoliated deciduous teeth, J. Biomed. Mater. Res. 105 (2017) 1083–1093, https://doi.org/10.1002/jbm.a.36003.
[27] F.M.R. Witjas, B.M. van den Berg, C.W. van den Berg, M.A. Engelse, T.J. Rabelink, Concise review: the endothelial cell extracellular matrix regulates tissue homeostasis and repair, STEM CELLS Transl Med 8 (2019) 375–382, https://doi.org/10.1002/sctm.18-0155.
[28] M. Assunção, D. Dehghan-Baniani, C.H.K. Yiu, T. Später, S. Beyer, A. Blocki, Cell-derived extracellular matrix for tissue engineering and regenerative medicine, Front Bioeng Biotechnol 8 (2020) 602009, https://doi.org/10.3389/fbioe.2020.602009.
[29] M.-K. Lee, S.-P. Lin, W.-C. HuangFu, D.-S. Yang, I.-H. Liu, Endothelial-derived extracellular matrix ameliorate the stemness deprivation during ex vivo expansion of mouse bone marrow-derived mesenchymal stem cells, PloS One 12 (2017), e0184111, https://doi.org/10.1371/journal.pone.0184111.
[30] A.P. Kusumbe, S.K. Ramasamy, R.H. Adams, Coupling of angiogenesis and osteogenesis by a specific vessel subtype in bone, Nature 507 (2014) 323–328, https://doi.org/10.1038/nature13145.
[31] C. Wan, J. Shao, S.R. Gilbert, R.C. Riddle, F. Long, R.S. Johnson, E. Schipani, T. L. Clemens, Role of HIF-1α in skeletal development, Ann Ny Acad Sci 1192 (2010) 322–326, https://doi.org/10.1111/j.1749-6632.2009.05238.x.
[32] E. Schipani, C. Maes, G. Carmeliet, G.L. Semenza, Regulation of osteogenesis-angiogenesis coupling by HIFs and VEGF, J. Bone Miner. Res. 24 (2009) 1347–1353, https://doi.org/10.1359/jbmr.090602.
[33] E.A. Jaffe, R.L. Nachman, C.G. Becker, C.R. Minick, Culture of human endothelial cells derived from umbilical veins. Identification BY morphologic and immunologic criteria, J. Clin. Invest. 52 (1973) 2745–2756, https://doi.org/10.1172/jci107470.
[34] B. Baudin, A. Bruneel, N. Bosselut, M. Vaubourdolle, A protocol for isolation and culture of human umbilical vein endothelial cells, Nat. Protoc. 2 (2007) 481–485, https://doi.org/10.1038/nprot.2007.54.
[35] G.D. Kusuma, M.C. Yang, S.P. Brennecke, A.J. O'Connor, B. Kalionis, D.E. Heath, Transferable matrixes produced from decellularized extracellular matrix promote proliferation and osteogenic differentiation of mesenchymal stem cells and facilitate scale-up, ACS Biomater. Sci. Eng. 4 (2018), https://doi.org/10.1021/acsbiomaterials.7b00747.
[36] F. Pati, J. Jang, D.-H. Ha, S.W. Kim, J.-W. Rhie, J.-H. Shim, D.-H. Kim, D.-W. Cho, Printing three-dimensional tissue analogues with decellularized extracellular matrix bioink, Nat. Commun. 5 (2014) 3935, https://doi.org/10.1038/ncomms4935.
[37] R.F. Nicosia, A. Ottinetti, Modulation of microvascular growth and morphogenesis by reconstituted basement membrane gel in three-dimensional cultures of rat aorta: a comparative study of angiogenesis in Matrigel, collagen, fibrin, and plasma clot, Vitro Cell Dev. Biol. 26 (1990) 119–128, https://doi.org/10.1007/bf02624102.
[38] I. Zein, D.W. Hutmacher, K.C. Tan, S.H. Teoh, Fused deposition modeling of novel scaffold architectures for tissue engineering applications, Biomaterials 23 (2002) 1169–1185, https://doi.org/10.1016/s0142-9612(01)00232-0.
[39] W. Zhang, W. Shi, S. Wu, M. Kuss, X. Jiang, J.B. Untrauer, S.P. Reid, B. Duan, 3D printed composite scaffolds with dual small molecule delivery for mandibular bone regeneration, Biofabrication 12 (2020), 035020, https://doi.org/10.1088/1758-5090/ab906e.
[40] M.A. Kuss, R. Harms, S. Wu, Y. Wang, J.B. Untrauer, M.A. Carlson, B. Duan, Short-term hypoxic preconditioning promotes prevascularization in 3D bioprinted bone constructs with stromal vascular fraction derived cells, RSC Adv. 7 (2017) 29312–29320, https://doi.org/10.1039/c7ra04372d.
[41] P.M. Crapo, T.W. Gilbert, S.F. Badylak, An overview of tissue and whole organ decellularization processes, Biomaterials 32 (2011) 3233–3243, https://doi.org/10.1016/j.biomaterials.2011.01.057.
[42] H. Lin, G. Yang, J. Tan, R.S. Tuan, Influence of decellularized matrix derived from human mesenchymal stem cells on their proliferation, migration and multi-lineage differentiation potential, Biomaterials 33 (2012) 4480–4489, https://doi.org/10.1016/j.biomaterials.2012.03.012.
[43] A. Honarvar, S. Karbasi, B. Hashemibeni, M. Setayeshmehr, M. Kazemi, A. Valiani, Effects of cartilage acellular solubilised ECM on physicomechanical and biological properties of polycaprolactone/fibrin hybrid scaffold fabricated by 3D-printing and salt-leaching methods, Mater. Technol. (2020) 1–9, https://doi.org/10.1080/10667857.2020.1824148.
[44] A.M. Jorgensen, Z. Chou, G. Gillispie, S.J. Lee, J.J. Yoo, S. Soker, A. Atala, Decellularized skin extracellular matrix (dsECM) improves the physical and biological properties of fibrinogen hydrogel for skin bioprinting applications, Nanomaterials-Basel 10 (2020) 1484, https://doi.org/10.3390/nano10081484.
[45] C. Piard, H. Baker, T. Kamalitdinov, J. Fisher, Bioprinted osteon-like scaffolds enhance in vivo neovascularization, Biofabrication 11 (2019), 025013, https://doi.org/10.1088/1758-5090/ab078a.
[46] Y. Jing, B. Yang, W. Yuan, S. Han, L. Song, M. Ye, Z.-Y. Zhang, L. Bian, Dynamic cell-adaptable hydrogels with a moderate level of elasticity promote 3D development of encapsulated cells, Appl Mater Today 22 (2021) 100892, https://doi.org/10.1016/j.apmt.2020.100892.
[47] Q. Rong, S. Li, Y. Zhou, Y. Geng, S. Liu, W. Wu, T. Forouzanfar, G. Wu, Z. Zhang, M. Zhou, A novel method to improve the osteogenesis capacity of hUCMSCs with dual-directional pre-induction under screened co-culture conditions, Cell Prolif 53 (2020), e12740, https://doi.org/10.1111/cpr.12740.
[48] Q. Li, W. Zhang, G. Zhou, Y. Cao, W. Liu, Z.-Y. Zhang, Demineralized bone matrix-based microcarrier scaffold favors vascularized large bone regeneration in vivo in a rat model, J. Biomater. Appl. 33 (2018) 182–195, https://doi.org/10.1177/0885328218784370.
[49] L. Wang, L. Zhu, Z. Wang, A. Lou, Y. Yang, Y. Guo, S. Liu, C. Zhang, Z. Zhang, H. Hu, B. Yang, P. Zhang, H. Ouyang, Z. Zhang, Development of a centrally vascularized tissue engineering bone graft with the unique core-shell composite structure for large femoral bone defect treatment, Biomaterials 175 (2018) 44–60, https://doi.org/10.1016/j.biomaterials.2018.05.017.
[50] L. Wang, H. Fan, Z.-Y. Zhang, A.-J. Lou, G.-X. Pei, S. Jiang, T.-W. Mu, J.-J. Qin, S.-Y. Chen, D. Jin, Osteogenesis and angiogenesis of tissue-engineered bone constructed by prevascularized β-tricalcium phosphate scaffold and mesenchymal stem cells, Biomaterials 31 (2010) 9452–9461, https://doi.org/10.1016/j.biomaterials.2010.08.036.
[51] S.K. Ramasamy, A.P. Kusumbe, L. Wang, R.H. Adams, Endothelial Notch activity promotes angiogenesis and osteogenesis in bone, Nature 507 (2014) 376–380, https://doi.org/10.1038/nature13146.
[52] K.D. Hankenson, M. Dishowitz, C. Gray, M. Schenker, Angiogenesis in bone regeneration, Injury 42 (2011) 556–561, https://doi.org/10.1016/j.injury.2011.03.035.
[53] M. Hendriks, S.K. Ramasamy, Blood vessels and vascular niches in bone development and physiological remodeling, Front Cell Dev Biology 8 (2020) 602278, https://doi.org/10.3389/fcell.2020.602278.
[54] J. Feng, L. Ye, Coupling between osteogenesis and angiogenesis, Faseb. J. 22 (2008), https://doi.org/10.1096/fasebj.22.1_supplement.233.2, 233.2-233.2.
[55] S. Zhu, S. Bennett, V. Kuek, C. Xiang, H. Xu, V. Rosen, J. Xu, Endothelial cells produce angiocrine factors to regulate bone and cartilage via versatile mechanisms, Theranostics 10 (2020) 5957–5965, https://doi.org/10.7150/thno.45422.

[56] Y. Peng, S. Wu, Y. Li, J.L. Crane, Type H blood vessels in bone modeling and remodeling, Theranostics 10 (2020) 426–436, https://doi.org/10.7150/thno.34126.
[57] R. Agarwal, A.J. García, Biomaterial strategies for engineering implants for enhanced osseointegration and bone repair, Adv. Drug Deliv. Rev. 94 (2015) 53–62, https://doi.org/10.1016/j.addr.2015.03.013.
[58] H. Xie, Z. Cui, L. Wang, Z. Xia, Y. Hu, L. Xian, C. Li, L. Xie, J. Crane, M. Wan, G. Zhen, Q. Bian, B. Yu, W. Chang, T. Qiu, M. Pickarski, L.T. Duong, J.J. Windle, X. Luo, E. Liao, X. Cao, PDGF-BB secreted by preosteoclasts induces angiogenesis during coupling with osteogenesis, Nat. Med. 20 (2014) 1270–1278, https://doi.org/10.1038/nm.3668.
[59] R.C. Riddle, R. Khatri, E. Schipani, T.L. Clemens, Role of hypoxia-inducible factor-1α in angiogenic–osteogenic coupling, J. Mol. Med. 87 (2009) 583–590, https://doi.org/10.1007/s00109-009-0477-9.
[60] S.J. Hollister, Porous scaffold design for tissue engineering, Nat. Mater. 4 (2005) 518–524, https://doi.org/10.1038/nmat1421.
[61] L. Wang, M. Zhao, S. Li, U.J. Erasquin, H. Wang, L. Ren, C. Chen, Y. Wang, C. Cai, "Click" immobilization of a VEGF-mimetic peptide on decellularized endothelial extracellular matrix to enhance angiogenesis, Acs Appl Mater Inter 6 (2014) 8401–8406, https://doi.org/10.1021/am501309d.
[62] T. Wang, Y. Zhai, M. Nuzzo, X. Yang, Y. Yang, X. Zhang, Layer-by-layer nanofiber-enabled engineering of biomimetic periosteum for bone repair and reconstruction, Biomaterials 182 (2018) 279–288, https://doi.org/10.1016/j.biomaterials.2018.08.028.
[63] F.B. Fernandez, S.S. Babu, M. Komath, H. Varma, Biointegration of Medical Implant Materials, 2020, pp. 245–261, https://doi.org/10.1016/b978-0-08-102680-9.00010-x.
[64] S. Özbek, P.G. Balasubramanian, R. Chiquet-Ehrismann, R.P. Tucker, J.C. Adams, The evolution of extracellular matrix, Mol. Biol. Cell 21 (2010) 4300–4305, https://doi.org/10.1091/mbc.e10-03-0251.
[65] Y.S. Kim, M. Majid, A.J. Melchiorri, A.G. Mikos, Applications of decellularized extracellular matrix in bone and cartilage tissue engineering, Bioeng Transl Med 4 (2019) 83–95, https://doi.org/10.1002/btm2.10110.
[66] I.G. Kim, M.P. Hwang, P. Du, J. Ko, C. Ha, S.H. Do, K. Park, Bioactive cell-derived matrices combined with polymer mesh scaffold for osteogenesis and bone healing, Biomaterials 50 (2015) 75–86, https://doi.org/10.1016/j.biomaterials.2015.01.054.
[67] A. Kumar, K.C. Nune, R.D.K. Misra, Biological functionality of extracellular matrix-ornamented three-dimensional printed hydroxyapatite scaffolds, J. Biomed. Mater. Res. 104 (2016) 1343–1351, https://doi.org/10.1002/jbm.a.35664.
[68] P. Das, Y.P. Singh, B.B. Mandal, S.K. Nandi, Chapter 10 Tissue-derived decellularized extracellular matrices toward cartilage repair and regeneration, Methods Cell Biol. 157 (2020) 185–221, https://doi.org/10.1016/bs.mcb.2019.11.005.
[69] A.B. Zarrini, M. Bozorgi, M. Khazaei, M. Soleimani, Decellularized extracellular matrices in bone tissue engineering: from cells to tissues, Mini-Review, Cell Tissue Biology 14 (2020) 399–406, https://doi.org/10.1134/s1990519x20060127.
[70] A. Abaci, M. Guvendiren, Designing decellularized extracellular matrix-based bioinks for 3D bioprinting, Adv Healthc Mater (2020) 2000734, https://doi.org/10.1002/adhm.202000734.
[71] J.C. Silva, M.S. Carvalho, R.N. Udangawa, C.S. Moura, J.M.S. Cabral, C.L. da Silva, F.C. Ferreira, D. Vashishth, R.J. Linhardt, Extracellular matrix decorated polycaprolactone scaffolds for improved mesenchymal stem/stromal cell osteogenesis towards a patient-tailored bone tissue engineering approach, J. Biomed. Mater. Res. B Appl. Biomater. 108 (2020) 2153–2166, https://doi.org/10.1002/jbm.b.34554.
[72] Z. Zheng, Y. Chen, D. Wu, J. Wang, M. Lv, X. Wang, J. Sun, Z.-Y. Zhang, Development of an accurate and proactive immunomodulatory strategy to improve bone substitute material-mediated osteogenesis and angiogenesis, Theranostics 8 (2018) 5482–5500, https://doi.org/10.7150/thno.28315.
[73] F. Pati, T.-H. Song, G. Rijal, J. Jang, S.W. Kim, D.-W. Cho, Ornamenting 3D printed scaffolds with cell-laid extracellular matrix for bone tissue regeneration, Biomaterials 37 (2015) 230–241, https://doi.org/10.1016/j.biomaterials.2014.10.012.
[74] R. Junka, K. Quevada, X. Yu, Acellular polycaprolactone scaffolds laden with fibroblast/endothelial cell-derived extracellular matrix for bone regeneration, J. Biomed. Mater. Res. 108 (2020) 351–364, https://doi.org/10.1002/jbm.a.36821.
[75] Y. Xu, B. Shao, X. Zeng, Z. Song, M. Jia, Z. Gong, Biofunctional ECM-PCL-HA scaffold and SMSCs/chondrocytes for repairing cartilage defects, Tissue Eng. (2020), https://doi.org/10.1089/ten.tea.2020.0245, 0.
[76] G.E. Davis, D.R. Senger, Endothelial extracellular matrix, Circ. Res. 97 (2005) 1093–1107, https://doi.org/10.1161/01.res.0000191547.64391.e3.
[77] R.O. Hynes, A. Naba, Overview of the matrisome—an inventory of extracellular matrix constituents and functions, Csh Perspect Biol 4 (2012) a004903, https://doi.org/10.1101/cshperspect.a004903.
[78] J.R. García, A.J. García, Biomaterial-mediated strategies targeting vascularization for bone repair, Drug Deliv Transl Re 6 (2016) 77–95, https://doi.org/10.1007/s13346-015-0236-0.
[79] H. Liu, Y. Du, G. Yang, X. Hu, L. Wang, B. Liu, J. Wang, S. Zhang, Delivering proangiogenic factors from 3D-printed polycaprolactone scaffolds for vascularized bone regeneration, Adv Healthc Mater 9 (2020), e2000727, https://doi.org/10.1002/adhm.202000727.
[80] J. Wang, C. Lin, X. Gao, Z. Zheng, M. Lv, J. Sun, Z. Zhang, The enhanced osteogenesis and osteointegration of 3-DP PCL scaffolds via structural and functional optimization using collagen networks, RSC Adv. 8 (2018) 32304–32316, https://doi.org/10.1039/c8ra05615c.
[81] J. Wang, D. Wu, Z. Zhang, J. Li, Y. Shen, Z. Wang, Y. Li, Z.-Y. Zhang, J. Sun, Biomimetically ornamented rapid prototyping fabrication of an apatite–collagen–polycaprolactone composite construct with nano–micro–macro hierarchical structure for large bone defect treatment, Acs Appl Mater Inter 7 (2015) 26244–26256, https://doi.org/10.1021/acsami.5b08534.
[82] Y. Yang, Y. Xiao, Biomaterials regulating bone hematoma for osteogenesis, Adv Healthc Mater 9 (2020) 2000726, https://doi.org/10.1002/adhm.202000726.